

Direct Numerical Simulation of bubble-induced turbulence at high Reynolds numbers

Alessio Innocenti¹, Alice Jaccod¹, Stéphane Popinet¹ and Sergio Chibbaro¹

¹Sorbonne Université, CNRS, UMR 7190, Institut Jean Le Rond d'Alembert, F-75005 Paris, France

(Received xx; revised xx; accepted xx)

We report on a numerical investigation of turbulent bubbly flows. Bubbles of a size larger than the small scales at which dissipation is efficient, cannot be treated as point-wise inclusions, and generate important hydrodynamic fields in the carrier fluid when in motion. In liquid-gas multiphase flows, buoyancy is the typical force which makes bubbles rise in the surrounding liquid. Furthermore, when the volume fraction of bubbles is important enough, the bubble motion may induce a collective agitation due to hydrodynamic interactions of the wakes which display some turbulent-like features. We tackle this complex phenomenon from a numerical point of view, performing direct numerical simulations (DNS) based on a Volume-of-fluid (VOF) method. Adaptive grids are used to make the computational effort feasible when needed.

In the first part of the work, we investigate several 2D and 3D tests for which either analytical or other numerical results are present. Specifically we have studied the rise of an array of bubbles. Particular attention has been paid to the effect of grid resolution and the value of the physical parameters, notably the density and viscosity ratio between the two phases. It is shown that in order to get accurate results, even from a qualitative point of view, it is key to carry out simulations with realistic physical parameters and well-resolved bubbles. These constraints are increasingly severe with increasing velocity of the bubbles.

In the second part, we focus on the dynamics of a bubble column in two and three dimensions. Bubbles initially placed at the bottom of the column rise freely afterwards. The configuration and the physical parameters are similar to those used in laboratory experiments, that is the Reynolds number based on bubble diameter is high. We have analysed both the spectra and the statistics of fluid velocity. In two dimensions, we have found that for high-enough Reynolds number an inverse cascade is produced for scales larger than the bubble diameter. At smaller scales viscous dissipation seems to dominate. In three dimensions, a cascade process has been found as in experiments which displays a k^{-3} slope for the energy spectrum as a function of the wavenumber. The mechanisms underlying the different cascades are unveiled by a local scale-by-scale analysis in physical space.

1. Introduction

Multiphase flows are ubiquitous in nature and represent one of the main subject of study in fluid mechanics (Prosperetti & Tryggvason 2009). Among the various kinds of multiphase flows, bubbly flows represent a challenging and key field of investigation, both for their fundamental dynamics and their numerous applications in engineering and

environmental science (Prosperetti 2004; Magnaudet & Eames 2000; Ern *et al.* 2012; Lohse 2018; Mathai *et al.* 2020).

Bubble columns are a particularly interesting configuration. Indeed they are conceptually simple: gas is injected at the bottom of a liquid-filled vessel and the bubbles rise due to buoyancy. High transfer rates can then be attained owing to the increased contact area between the gas and the liquid phases, and to the liquid agitation induced by bubble motion. These efficient heat and mass transfer characteristics make bubble columns useful as industrial devices. They are also a good configuration to analyse the fundamental features of bubble dynamics, as highlighted in the pioneering work of Lance & Bataille (1991). Since a reliable prediction of bubble residence time and available interfacial area is crucial for an accurate design of industrial devices, the understanding of bubble flow dynamics is essential. In particular, due to the large density difference between gases and liquids. Under the effect of buoyancy the bubbles rise with a velocity considerably different from that of the liquid. They thus induce velocity disturbances in the liquid that collectively generate a complex agitation. In generic flows, this bubble-induced agitation, also called pseudo-turbulence, is often coupled to a turbulent agitation inherent to the liquid phase. The understanding of the pure bubble-induced agitation, without a previous turbulent motion of the liquid, is key to grasp the physics of more complex flows.

For this reason several experimental studies have been carried out to investigate this particular regime in different configurations (Zenit *et al.* 2001; Martínez-Mercado *et al.* 2007; Riboux *et al.* 2010). This research has highlighted some characteristics of bubble-induced agitation. In the case of a single bubble, it has been shown that the average rise velocity is a non-monotonic function of the diameter and, more surprisingly, that path instability may occur, producing complex oscillating trajectories (Mougin & Magnaudet 2001; Ern *et al.* 2012). Furthermore, the bubble produces a velocity disturbance in the surrounding fluid. In particular, at large Reynolds numbers, a flow disturbance that decays as r^{-3} (Batchelor 2000), and a wake whose mean velocity decays with the vertical distance from the bubble z as z^{-1} in a laminar flow (Landau & Lifshitz 1987; Batchelor 2000) and as $z^{-2/3}$ in a turbulent one (Landau & Lifshitz 1987). This is an important fact, since it means that the superposition of non-interacting bubbles leads to the divergence of the variance of the liquid velocity with the number of bubbles. However, it is an experimental evidence (Risso & Ellingsen 2002) that at moderate-to-large Reynolds numbers ($Re \gtrsim 100$) there is no such divergence of the velocity variance because the wakes of interacting bubbles are attenuated. That shows that at large Reynolds numbers the dominant mechanism underlying liquid agitation is the nonlinear wake interaction. Therefore, the results obtained with a small number of bubbles which interact only weakly are of little relevance to understand large-Reynolds number flows, typical of experiments.

When many bubbles are present, the main phenomenology is the following (Risso 2018): (i) At variance with particle-laden flows (Toschi & Bodenschatz 2009; Balachandar & Eaton 2010), no significant clustering is observed, when homogeneous swarms of spherical bubbles are considered. (ii) The average rise velocity of the bubbles is lower than in the isolated bubble case, and the dependence on the volume fraction is still unclear. (iii) Bubble velocity fluctuations seem to present a strong asymmetry between horizontal and vertical fluctuations. (iv) The agitation of the liquid clearly increases with the bubble volume fraction. Its energy spectrum ($E(k)$) appears to display a crossover between a steeper ($E \sim k^{-3}$) slope at large scales and a milder one at small scales ($E \sim k^{-5/3}$). (v) The probability density function (PDF) of the vertical fluctuations is strongly skewed and thus non-Gaussian, while the horizontal one is symmetric and closer to Gaussian.

These characteristics have been revealed through important experiments which are far from being easy. For instance, it is difficult to avoid any external effects on the

swarm, to impose precise homogeneous conditions and monodispersity. Furthermore, even though the measurement tools have been largely improved in the last decades, not all the above statements have the same robustness. In particular, measurements of the bubble and liquid fluctuations are very difficult and surely affected by large errors. Hence, an assessment of the above phenomenology is still important. Furthermore, some of the physical mechanisms that cause these dynamics are still to be described. Notably, the scale dependence of the spectrum remains unclear and the precise mechanism underlying the turbulence production is not known.

From the above consideration, it seems clear that numerical experiments, *i.e.* direct numerical simulations (DNS), of such flows are highly attractive since they allow to analyse idealised configurations and, thus, complement the experiments to understand the fundamental physics. They can also provide key data in view of the development of more approximate models. For such reasons, huge efforts have been made to develop efficient numerical approaches in the last decades (Tryggvason *et al.* 2011). In particular, numerical simulations of columns of few tens of bubbles in channel flows have been carried out in many configurations at moderate Re number (Esmarelli & Tryggvason 1998, 1999, 2005), and more recently some tentatives have been made to simulate homogeneous swarms at higher Reynolds number with very few bubbles (Roghair *et al.* 2011, 2013).

However, several issues affect DNS of bubbly flows. As has been said before, the numerical experiments must consider a sufficiently large number of interacting bubbles to represent soundly the dynamics of realistic flows at high Reynolds numbers. Secondly, it has been clearly pointed out in a recent important work (Cano-Lozano *et al.* 2016a) that under-resolving the bubble dynamics, *i.e.* using an insufficient number of mesh nodes to describe each bubble, dramatically affects the results obtained. The differences between *real* DNS of bubbly flows and under-resolved numerical simulations are unfortunately not only quantitative but also qualitative, which means that under-resolved simulations fail to capture even the various regimes of the flow. Moreover, in the cited work a large campaign on numerical simulations neatly indicates that the number of points required to discretize the problem grows almost linearly with the bubble Re number. The final drawback of DNS is that, as in general for numerical simulations of turbulent flows (Pope 2000), yet even more truly for multiphase flows, it is difficult to achieve Reynolds numbers as large as those obtained in experiments. Furthermore, we shall show in this work, that having realistic values of the surface tension and of the density ratio between the liquid and gas phases is also necessary to avoid spurious effects. In the light of such constraints, while simulations carried out at small Re can be considered with confidence, a well-resolved DNS of bubble swarm at high Re is still missing.

The first objective of this work is precisely to present the results of the first well-resolved DNS of a bubble column at high Re .

Concerning the phenomenology, the issue of the dependence of the rise velocity on the bubble volume fraction has been recently addressed in the case of moderate Re and with ordered arrays, which can be simulated using a single bubble (Loisy *et al.* 2017). We will assess some of those results using a different numerical approach. On the other hand, our main aim will be to characterise the statistical properties of the flow, using both two-dimensional and three-dimensional configurations. Notably, we compute the statistics in the region below the bubble swarm, as done in experiments (Riboux *et al.* 2010). Both energy distribution and velocity PDFs will be analysed.

2. Mathematical formulation

2.1. Problem statement

We investigate the dynamics of a monodisperse suspension of bubbles rising under the action of buoyancy in a fluid initially at rest. The density, the viscosity and the surface tension of each fluid are considered constant during each numerical experiment. The gravity is assumed to be always aligned with the vertical direction and the possible influence of the orientation of the gravity is out of the scope of the present work. Different configurations of increasing difficulty are studied. We first consider an infinite homogeneous suspension, which is represented by the periodic repetition of cubic unit cells containing a given number of bubbles. When a single bubble is considered, this describes an ordered array of bubbles. We then consider a more realistic configuration in which a given number of bubbles are initially randomly distributed at the bottom of a channel and rise through it. This problem is analyzed in two dimensions while varying several parameters and is then studied in three dimensions at high Reynolds number.

Many physical parameters may characterize the problem: the gas volume fraction ϕ , the number of bubbles N_b , the diameter of the bubbles d_b calculated as the diameter of the sphere of equivalent volume, the gravity acceleration g , the viscosity of the two fluids μ_b , μ_l , their densities ρ_b , ρ_l , and the surface tension σ . We use the subscripts b for bubbles and l for liquid. Generally, the problem is physically described in terms of dimensionless groups. Four dimensionless groups can be formed in addition to the number of bubbles and the volume fraction. Two are the density and viscosity ratio $\frac{\rho_b}{\rho_l}$ and $\frac{\mu_b}{\mu_l}$. We briefly analyse the impact of the density ratio but in almost all simulations we have fixed $\rho_b/\rho_l = 10^{-3}$ and $\mu_b = \mu_l = 10^{-2}$, which are typical values for air bubbles in water.

The other two dimensionless groups can be characterised by the Galileo number

$$Ga \equiv \frac{\rho_l |\Delta\rho| g d_b^3}{\mu_l^2}, \quad (2.1)$$

where $\Delta\rho = \rho_b - \rho_l$, or equivalently the Archimedes number $Ar \equiv \sqrt{Ga}$, and the Bond (or Eötvös) number

$$Bo \equiv \frac{|\Delta\rho| g d_b^2}{\sigma} \quad (2.2)$$

These numbers indicate the importance of buoyancy and surface tension and do not include the velocity of the bubble.

When bubbles move, a typical velocity scale has to be added to the relevant quantities. We compute the evolution with time of the (space-)averaged velocity of each phase. We note the average bubble velocity $\langle U_b \rangle$. It is then possible to define the bubble Reynolds number based on this velocity

$$Re \equiv \frac{\langle U_b \rangle d_b}{\nu_l}, \quad (2.3)$$

where ν_f is the kinematic viscosity of the liquid. It is also possible to use another group which compares the dynamic effects with the surface tension, the Weber number

$$We \equiv \frac{\rho_b \langle U_b \rangle^2 d_b}{\sigma} = \frac{Bo Re^2}{Ga}. \quad (2.4)$$

It is important to note that the average bubble velocity may or may not reach a stationary state in our numerical experiments, so that in general the dynamic dimensionless numbers are dependent on time $Re = Re(t)$.

In the first part of this work, we analyse the relation $U = U(N_b, \phi, Bo, Ga)$ and compare the results with recent numerical studies obtained with different methods, and with analytical solutions whenever possible. We will also measure the influence of the density ratio, notably on the rate of coalescence. In the second part, we will study the phenomenology of some realistic configuration with the parameters set as in typical experiments.

2.2. Governing equations

Both fluids are governed by the Navier–Stokes equations, which we take here in the incompressible limit

$$\nabla \cdot \mathbf{u}_i = 0 \quad (2.5)$$

$$\frac{\partial \mathbf{u}_i}{\partial t} + \nabla \cdot (\mathbf{u}_i \otimes \mathbf{u}_i) = \frac{1}{\rho_i} (-\nabla p_i + \nabla \cdot (2\mu_i \mathbf{D}_i)) + \mathbf{f}_i, \quad (2.6)$$

where $\mathbf{D}_i = [\nabla \mathbf{u}_i + (\nabla \mathbf{u}_i)^T]/2$ is the symmetric deformation tensor, the subscript i indicates each phase $i = b, l$, and \mathbf{f}_i represents the acceleration due to volume forces, which in the present case are the gravity, $\mathbf{f}_i = \mathbf{g}$.

In addition, the appropriate boundary conditions at the interface between the phases are to be imposed. Since we do not consider any phase change, the interfacial condition for viscous fluids is simply $\mathbf{u}_b = \mathbf{u}_l$, or

$$[\mathbf{u}]_S = 0, \quad (2.7)$$

where we have used the jump notation, *i.e.* the notation $[x]_S = x_b - x_l$. When the surface tension is constant, as considered in the present work, the normal stress displays a discontinuity at the interface, whereas the shear stress is continuous. The jump at the interface is given by

$$[p] = \sigma \kappa \mathbf{n}, \quad (2.8)$$

where \mathbf{n} is the unit normal vector defined as directed outward from the bubbles, and κ is the mean curvature of the interface. This set of equations are solved through the code Basilisk[†] with the numerical methods described in the following section. In particular, the accurate numerical calculation of the surface tension is key in multiphase flows (Popinet 2018).

3. Numerical method

Basilisk is an ensemble of solvers written using an extension to the C programming language, called Basilisk C, useful to write discretization schemes on Cartesian grids (see <http://basilisk.fr>). Space is discretized using a Cartesian (multi-level or tree-based) grid where the variables are located at the center of each control volume (a square in 2-D, a cube in 3-D) and at the center of each control surface. The possibility to adapt the grid dynamically is key to efficiently simulate multiphase flows (Popinet 2009). Two primary criteria are used to decide where to refine the mesh. They are based on a wavelet-decomposition of the velocity and volume fraction fields respectively (van Hooft *et al.* 2018). The velocity criterion is mostly sensitive to the second-derivative of the velocity field and guarantees refinement in developing boundary layers and wakes. The volume fraction criterion is sensitive to the curvature of the interface and guarantees the accurate description of the shape of bubbles. Both criteria are usually combined with

[†] <http://basilisk.fr>

a maximum allowed level of refinement. As demonstrated in previous work, using the earlier code Gerris (Cano-Lozano *et al.* 2016a), this strategy leads to very large savings in computational cost compared to fixed Cartesian grid approaches.

The numerical scheme implemented in Basilisk is very close to that used in Gerris as described in Popinet (2009) and many other articles. The Navier–Stokes equations are integrated by a projection method (Chorin 1969). Standard second-order numerical schemes for the spatial gradients are used (Popinet 2003, 2009; Lagr  e *et al.* 2011). In particular, the velocity advection term $\partial_j(u_j u_i)^{n+1/2}$ is estimated by means of the Bell–Colella–Glaz second/third-order unsplit upwind scheme (Popinet 2003). In this way, the problem is reduced to the solution of a 3D Helmholtz–Poisson problem for each primitive variable and a Poisson problem for the pressure correction terms. Both the Helmholtz–Poisson and Poisson problems are solved using an efficient multilevel solver (Popinet 2003, 2015).

Time is advanced using a second-order fractional-step method with a staggered discretization in time of the velocity and scalar fields (Popinet 2009): one supposes the velocity field to be known at time n and the scalar fields (pressure, temperature, density) to be known at time $n - 1/2$, and one computes velocity at time $n + 1$ and scalars at time $n + 1/2$.

The interface between the fluids is tracked with a geometric Volume-Of-Fluid method (Hirt & Nichols 1981; Scardovelli & Zaleski 1999). The surface tension term is computed using an accurate well-balanced, height-function method (Popinet 2018).

Periodic, no-slip and free-slip boundary conditions will be imposed in the different computations considered.

4. Arrays of bubbles

4.1. Validation tests

To assess the accuracy of the numerical code for the simulation of two-phase bubbly flows, we have reproduced several literature test cases (Esmaeeli & Tryggvason 1998, 1999; Sangani 1987) which have been considered very recently with another numerical approach (Loisy *et al.* 2017). In particular we have focused on the configuration of arrays of rising bubbles, which, in the presence of gravity, start to rise inside a heavier fluid at rest, due to buoyancy. After an initial transient where bubbles accelerate, they eventually reach a quasi-steady-state regime. Depending on bubble size, surface tension and density, they may follow non-rectilinear paths, with periodic or chaotic lateral oscillations (Cano-Lozano *et al.* 2016a). All benchmark tests consist in a regular array of bubbles, which is reproduced numerically using a single bubble in a periodic cell. Changing the cell size with respect to the bubble size, we can adjust the volume fraction of the array. Note that since the computational domain is unbounded in all directions, an additional body force $-\langle\rho\rangle g$ must be added to avoid that the system accelerates in the vertical downward direction.

As a first validation, we reproduced the simulations of Esmaeeli & Tryggvason (1998) of a 2-dimensional array of rising bubbles with the following non-dimensional numbers:

$$Ar = 5.6 \quad Bo = 1 \quad \rho_b/\rho_l = 0.05 \quad \mu_b/\mu_l = 0.05$$

The volume fraction is $\varphi = 0.125$. A regular grid with different levels of refinement has been tested to check the convergence of the numerical code. The details of the different grids (total number of grid points N , and number of grid points-per-bubble diameter, d_b/Δ) are reported in table 1. Figure 1 shows the bubble Reynolds number

| | |
|-------------------------------------|---|
| N | 32 ² 64 ² 128 ² 256 ² |
| d_b/Δ | 12.5 25 50 100 |
| Re_f (present) | 1.55 1.491 1.456 1.439 |
| Re_f Esmaeeli & Tryggvason (1998) | 1.375 1.41 1.42 \ |

Table 1: Grid resolutions for the 2-D array of bubbles of Esmaeeli & Tryggvason (1998)

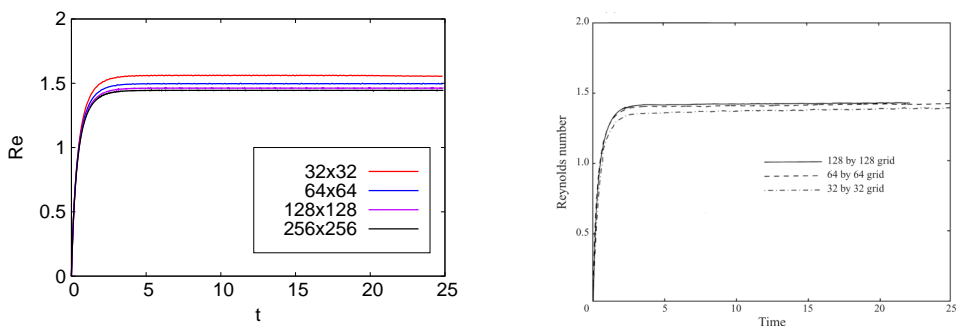


Figure 1: Time evolution of the Reynolds number of the rising deformable bubbles at moderate Reynolds number for the 2D configuration, for different grid resolutions. Present results on the left panel, DNS by Esmaeeli & Tryggvason (1998) on the right panel.

$Re = (\rho_l U_b d_b) / \mu_l$ for the actual computation compared to figure 1 of Esmaeeli & Tryggvason (1998). The transient rise is reproduced accurately, with the Reynolds attaining its steady value at approximately $t = 3$. We show here also that the 64² grid is not fully converged as in Esmaeeli & Tryggvason (1998), but the steady value of Re for the converged grid (128²) is in good agreement, as shown in Table 1.

We have tested the numerical code also for moderate Reynolds numbers, reproducing the test case proposed by Esmaeeli & Tryggvason (1999). For this case the flow parameters are

$$Ar = 29.9 \quad Bo = 2 \quad \rho_b / \rho_l = 0.1 \quad \mu_b / \mu_l = 0.1.$$

The details of the different grids are reported in table 2. Results are shown in figure 2, where they are compared against both the original DNS and the more recent one (Esmaeeli & Tryggvason 1999; Loisy *et al.* 2017). We have used a more refined grid with respect to both other DNS to test the convergence in a rigorous way. We have found, as for the 2D case, that the grid convergence is not achieved with the number of points given in previous works (Esmaeeli & Tryggvason 1999; Loisy *et al.* 2017), where the authors indicate that 30 points for diameter are sufficient.

We have also compared our simulations with the theory of Sangani (1987) for the Stokes flow regime. The configuration consists in a cubic array of spherical bubbles at different volume fractions. The resolution adopted for this test case is $d_b/\Delta = 40$ and the non-dimensional numbers of the simulation are the same as in previous DNS studies,

| | | | | | |
|-------------------------------------|--|-----------------|-----------------|-----------------|------------------|
| N | | 16 ³ | 32 ³ | 64 ³ | 128 ³ |
| d_b/Δ | | 10 | 20 | 40 | 80 |
| Re_f (present) | | 23.05 | 22.01 | 21.275 | 21 |
| Re_f (Esmaeeli & Tryggvason 1998) | | \ | \ | 20.49 | \ |
| Re_f (Loisy <i>et al.</i> 2017) | | 19.05 | 20.22 | 20.58 | \ |

Table 2: Grid resolutions and final Reynolds for the 3-D array of bubbles of Esmaeeli & Tryggvason (1999).

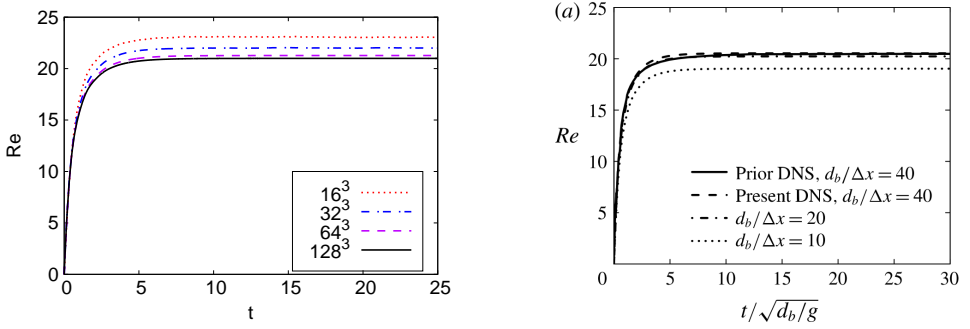


Figure 2: Time evolution of the bubble Reynolds number for different grid resolutions, for the 3D configuration. Present results on the left panel, Loisy *et al.* results on the right panel. In the right panel "prior DNS" stands for Esmaeeli *et al.*, while present DNS for Loisy *et al.*.

| $\phi^{1/3}$ | $ U/U_0 \text{ DNS} $ | $ U/U_0 \text{ Analytical} $ | relative error | d_b/Δ |
|--------------|-----------------------|------------------------------|----------------|--------------|
| 0.2 | 0.768 | 0.755 | 1.7% | 63.5 |
| 0.3 | 0.651 | 0.632 | 2.5% | 47.64 |
| 0.4 | 0.525 | 0.51 | 3 % | 63.5 |
| 0.5 | 0.408 | 0.39 | 4.3% | 79.4 |

Table 3: .

namely:

$$Ar = 0.15 \quad Bo = 0.38 \quad \rho_b/\rho_l = 0.005 \quad \mu_b/\mu_l = 0.01.$$

In Table 3 we show the steady state velocity of the bubble array normalized with the velocity of a single isolated bubble, and the quantitative numerical error. The agreement

| Case | Ar | Bo | ϕ |
|------|------|------|--------|
| a | 29.9 | 2 | 0.008 |
| b | 40.7 | 0.38 | 0.13 |
| c | 40.7 | 0.38 | 0.038 |

Table 4: Non-dimensional parameters for the 3D-oblique test case.

between the numerical and the analytical solution $\frac{U}{U_0} = 1 - 1.1734\mu^*\phi^{1/3} + O(\phi)$, is quite good.

4.2. 3-D oblique rise of bubbles

The last set of test cases is the oblique rise of periodic arrays of bubbles performed by Loisy *et al.* (2017). More specifically, the experiment consists in initializing a perfectly regular lattice of bubbles and follow its evolution. The lattice should be large enough (in principle infinite) to minimise boundary effects. From a numerical point of view, using periodic boundary conditions it is possible to simulate this test case with a single bubble. The volume fraction can be varied by changing the size of the bubble relative to the cell size. Loisy *et al.* (2017) pointed out that for certain values of the non-dimensional parameters, bubbles can experience an oblique trajectory (not aligned with gravity) at certain volume fractions, although a single bubble in the same parameter regime would follow a straight vertical path. Analytical considerations support the possibility of a non-trivial path indicating a possible transition for $Ar \approx 20$. In particular three different oblique regimes have been found: (a) a steady oblique rise, (b) an oscillatory oblique rise, with a bubble oscillating around a straight oblique path, and (c) a chaotic oblique rise. Such a behaviour had been previously noticed numerically (Sankaranarayanan *et al.* 2002), but using a diffuse interface method and a small density ratio.

In the present work we have simulated the configurations corresponding to the three regimes in Loisy *et al.* (2017) with a slightly increased resolution, to test if our numerical approach confirms these previous results. The parameters of the simulations are reported in table 4. The density ratio and the viscosity ratio between the two phases are the same for all the cases, $\rho_b/\rho_l = 0.005$, $\mu_b/\mu_l = 0.01$. The number of points is varied with the domain size in order to get always the same bubble resolution $d_b/\Delta = 40$ for all cases. Results are shown in figures 3-4, where for each regime we compare our results to those of previous DNS by Loisy *et al.* (2017), and summarised in table 5.

Similar regimes are captured in each case, while the transition may occur at a different time with respect to Loisy *et al.* (2017), since it is triggered by numerical asymmetry. For the same reason, while we expect a quantitative agreement in the direction of gravity, the other two components can share the energy in a different way, provided that this is compatible with the symmetry of the problem. The steady value of the different components of the bubble Reynolds number is in excellent agreement for cases (a) and (b), while in case (c) where a steady regime is not reached, we can quantify the accuracy by comparing the oscillation period.

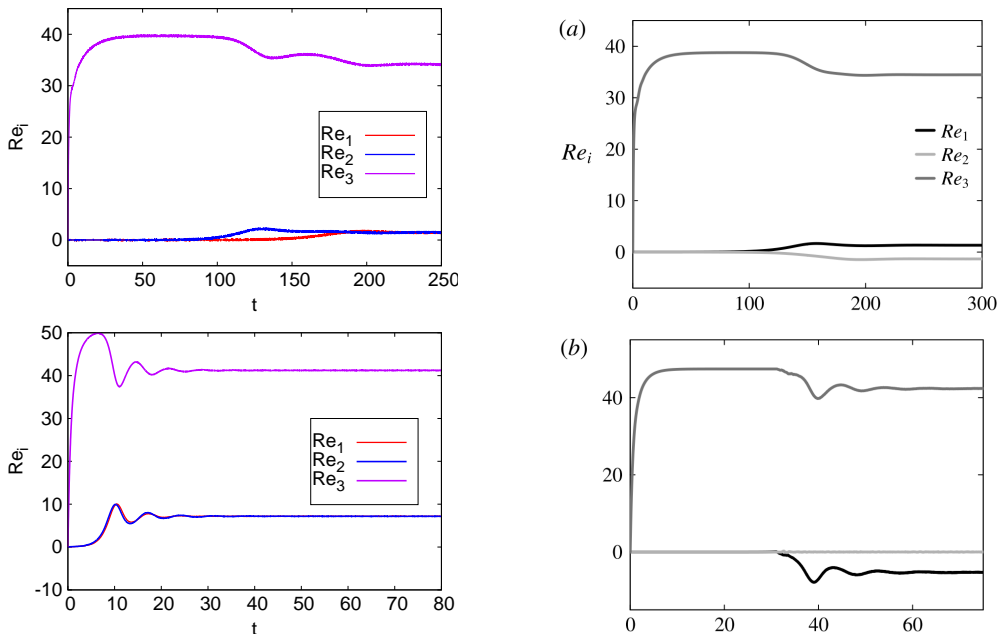


Figure 3: Time evolution of two components of the bubble Reynolds number for two different cases of steady oblique rise. Present results on the left panel, DNS by (Loisy *et al.* 2017) on the right panel.

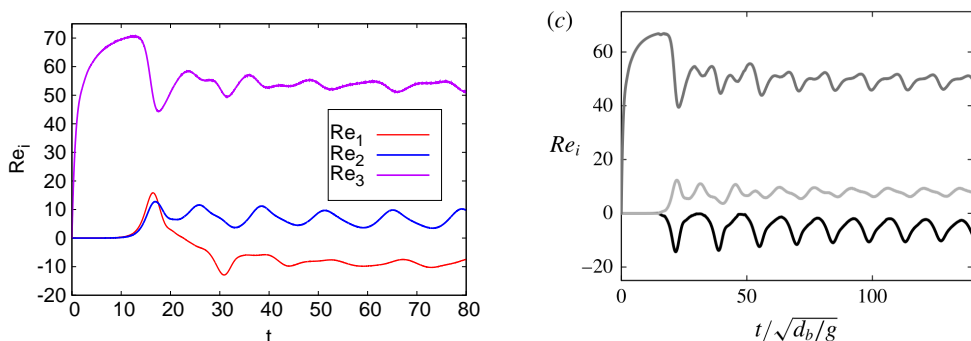


Figure 4: Time evolution of the three components of the bubble Reynolds number for regime (c), oscillatory oblique rise. Present results on the left panel, DNS by (Loisy *et al.* 2017) on the right panel.

5. Technical issues

In the previous section, we have analysed some cases of ordered arrays of bubbles to validate the numerical approach and compared with recent simulations carried out with a different method. In this section, we pursue the technical analysis, considering some issues which are crucial from a computational point of view and may significantly alter the results of the simulations of turbulent multiphase flows. In particular, we have seen that the density ratio between the two phases is generally very high (about 1000) in realistic flows. That brings a considerable computational effort to guarantee the convergence of

| Case | a | b | c |
|-----------------------------------|------|-------|------|
| Re_1 (present) | 34.1 | 41.2 | 52 |
| Re_1 (Loisy <i>et al.</i> 2017) | 34.4 | 42.2 | 50.1 |
| Re_3 (present) | 1.41 | 7.15 | -8.5 |
| Re_3 (Loisy <i>et al.</i> 2017) | 1.4 | -4.15 | -8.1 |

Table 5: Final Re for the 3D-oblique test case. For the last oscillating case we have reported the average over the last steps, so that the comparison is to be considered qualitative.

the method, and therefore it may be tempting to use smaller ratios in order to speed up simulations, considering the complexity of multiphase flows. In some cases, the correct physics can be reproduced with a density ratio well below the realistic value (Diotallevi *et al.* 2009), but that cannot be claimed in general. This is clearly a key issue for direct numerical simulations of multiphase flows.

The other issue we will analyse is the impact of the grid refinement. While convergence tests have been made for all the previous test cases, it is still useful to investigate this point in more complex configurations. Indeed, multiphase flows at high Reynolds numbers cannot be trustfully reproduced without a sufficient resolution (Cano-Lozano *et al.* 2016a). This issue thus deserves particular attention.

5.1. Coalescence

We first study from a qualitative point of view the coalescence of two bubbles. The study of fluid particle dynamics (coalescence and breakup) is of continuous interest because of its relevance to many industrial applications involving multiphase flow. In effect, it has been empirically shown that the dynamics of bubbly flows may be dependent on coalescence and breakup, which changes the distribution of diameters and numbers of bubbles. Together with breakup and mass transfer, coalescence is responsible for the evolution of drop and bubble sizes in multiphase flows. Compared to breakup, coalescence is considered more complex, since it involves not only interactions of bubbles with the surrounding liquid, but also interactions between bubbles themselves once they are brought together by the external flow or by body forces. This is a vast area of research (Liao & Lucas 2010) and a detailed analysis of this issue is out of the scope of the present work. However, it is important to have some control on this process to avoid spurious effects. It also constitutes an interesting configuration to test the influence of the numerical setup.

Generally speaking, present attempts to carry out DNS of bubbly flows may use methods which prevent coalescence entirely (Tryggvason *et al.* 2011; Loisy *et al.* 2017). This is convenient from a practical point of view, but cannot be considered entirely satisfactory since in general turbulent flows, in presence of buoyancy, coalescence may happen. On the contrary, VOF methods, like that used in the present work, tend to make coalescence too easy (Scardovelli & Zaleski 1999), if numerical parameters are not well controlled. In a recent work, coalescence has been observed in VOF simulations of

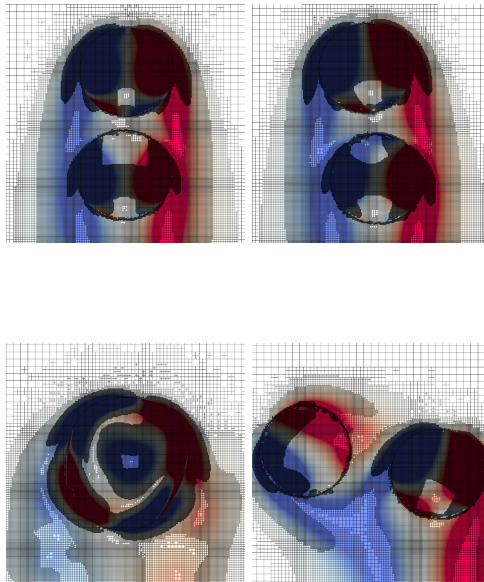


Figure 5: Contour plot of the vorticity at two instants. The grid is drawn to show the degree of refinement. Left column: simulation with $\rho_l/\rho_b = 100$; Right column: simulation with $\rho_l/\rho_b = 1000$.

turbulent bubbly flows (Dodd & Ferrante 2016), but the issue of a possible spurious impact of the numerics has not been considered.

Here we consider for this purpose two bubbles in a two-dimensional box of side 20 times the diameter of the bubbles with periodic boundary conditions. The physical parameters are fixed in such a way that dimensionless numbers are $Ar = 30$, $Bo = 0.1$ and $\mu_b/\mu_l = 100$. Unfortunately, due to the limited understanding of the processes underlying coalescence, empirical correlations are still needed. To date, no satisfactory models taking into account all mechanisms and applicable to a wide range of conditions are available in the literature (Jakobsen *et al.* 2005). Based on physical intuition and empirical evidence, the rate of coalescence depends on the diameters of the bubbles, their relative velocity and the turbulent rate of energy dissipation in turbulent flows. We consider two bubbles, one on top of the other, initially at rest in a quiescent fluid. The top bubble is at 0.75 diameter from the bottom bubble. They start moving because of buoyancy which induces vorticity fluctuations and creates wakes. From a physical point of view, those are the mechanisms which bring bubbles together and, with a certain probability, make them coalesce. With the physical parameters and initial conditions chosen, the probability of coalescence is not zero but quite low, on the basis of standard empirical models (Prince & Blanch 1990). Hence we shall consider our numerical approach satisfying if coalescence is avoided in this case. In figure 5, we show three instants of these dynamics, displaying also the vorticity field, for the first configuration studied. In this case, as highlighted in the figure, we have used a very high refinement of the grid, with a maximum refinement for the adaptive grid of 2^{13} points, which we are sure to be at convergence. Thus, we can assess the influence of the density ratio without other possible parameters at play.

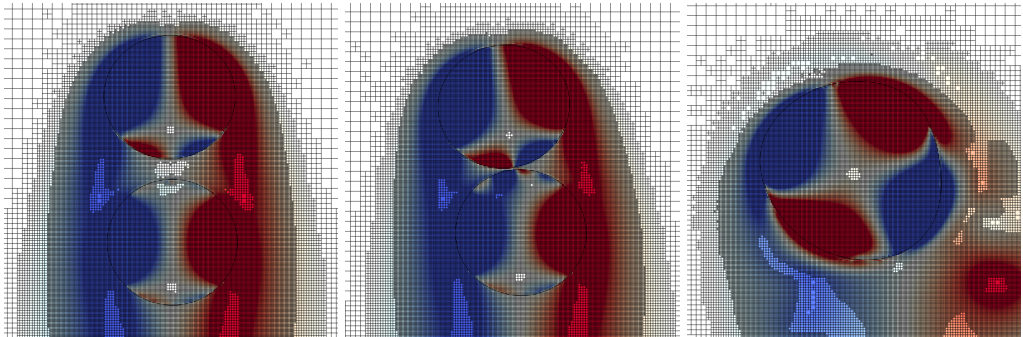


Figure 6: Contour plot of the vorticity at three instants. The grid is drawn to show the degree of refinement. It is possible to see that even with the present grid which is well refined ($N_{\text{Max}} = 2^{11}$) some details of the wake and of the film surrounding the bubbles are lost with respect to the more refined simulations displayed in Fig. 5 right column.

In the left column of the figure we plot the results obtained considering a density ratio of $\rho_l/\rho_b = 100$, for which coalescence happens. The coalescence process appears to go forward following several subprocesses, as expected by the theory: (1) the two bubbles collide, trapping a small amount of liquid between them; (2) bubbles keep in contact till the liquid film drains out to a critical thickness; (3) the film ruptures resulting in coalescence. Our simulations seem to indicate that in this particular case, dominated by buoyancy the coalescence happens following the classical drainage model (Shinnar & Church 1960). Indeed turbulent fluctuations and relative velocity are not sufficient to trigger a faster process. In the right column, we show the same case but with a density ratio of $\rho_l/\rho_b = 1000$. In this case, coalescence does not occur. We have investigated different density ratios in the range $\rho_l/\rho_b \in [10, 1000]$ (not shown here for the sake of clarity), and it turns out that the threshold for coalescence is about $\rho_l/\rho_b = 500$. Our results therefore point out that to reproduce multiphase flows, a realistic density ratio is mandatory, while it possibly may be slightly less than the actual one.

We now focus on the influence of grid refinement. We have carried out the simulation of the same test case with a density ratio $\rho_l/\rho_b = 1000$, with different grids, coarser than the previous one that had a maximum refinement of $N_{\text{Max}} = 2^{13}$ points. We have found that convergence is attained with $N_{\text{Max}} = 2^{12}$, when the results are the same as those obtained with $N_{\text{Max}} = 2^{13}$, and shown in figure 5. As shown in figure 6, with $N_{\text{Max}} = 2^{11}$ the coalescence occurs even with the correct density ratio. Furthermore, we can see from figure 6 that both the mechanisms and the typical time-scales of the process leading to coalescence are the same as those displayed in the left column of figure 5, for a much lower density ratio $\rho_l/\rho_b = 100$. In particular, the vorticity field at the end of the process appears to be almost identical. This means that, as far as coalescence rate is concerned, a coarse resolution may act in a similar way to a low density ratio. It is important to underline here that the strong influence of grid resolution is related to the high Ar number used in the simulations, which leads to the formation of thin viscous boundary layers.

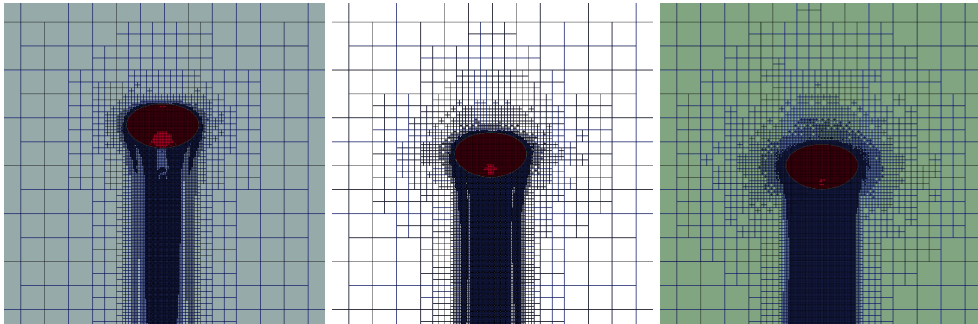


Figure 7: The vorticity field is displayed together with the mesh for three choices of the grid resolution, namely we have changed the error threshold as $e_v = 0.001; 0.003; 0.01$, in absolute value.

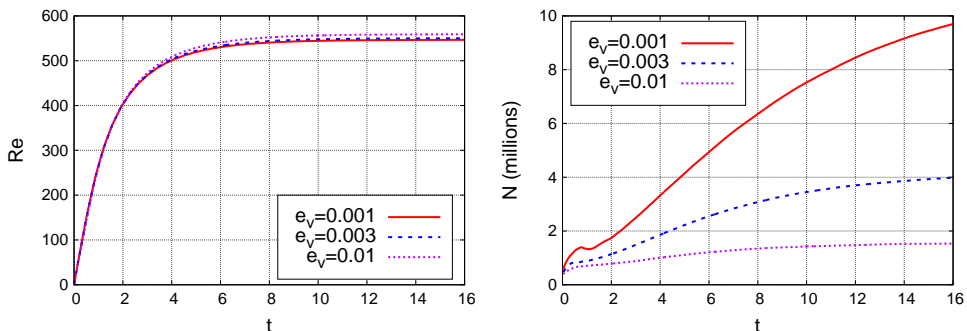


Figure 8: (a) The average Reynolds are plotted for the three resolutions. The final values are: $Re = 559$ for $e_v = 0.01$, $Re = 549$ for $e_v = 0.003$ and $Re = 547$ for $e_v = 0.001$. (b) The number of mesh points is plotted against time. It should be noted that the number of points is approximately steady for the two coarser resolutions, while it is growing rapidly for the most refined resolution.

5.2. Grid refinement effects

We have then studied in a more quantitative way the impact of the resolution. To do that, we have replicated the results obtained by Cano-Lozano *et al.* (2016a) to study the behaviour of a single bubble rising “in a large tank” i.e. far from any boundaries. We have used only the physical parameters that we would like to use for the realistic bubble column. Namely, we fix $Ar = 185$ and $Bo = 0.28$. The acceleration of gravity is set to unity, which gives a characteristic rise velocity also of order unity, which gives a maximum time for the simulation comparable to the domain size. In this regime, it turns out that bubble trajectories are between the rectilinear and chaotic regimes, as found in the original paper (Cano-Lozano *et al.* 2016a).

As shown in figure 7, we have simulated the bubble rise with three different grids. The maximum resolution allowed is always the same, $N_{Max} = 2^{12}$ such that the maximum refinement is of 82 points per diameter. However, we have performed three different simulations, varying the threshold of the error tolerance in the velocity (van Hooft *et al.* 2018), namely fixed at $err_v = 0.001; 0.003; 0.01$, in absolute value.

From figure 7, it is possible to see that for the large error tolerance, the neighbourhoods of the wake region and the bubble are discretized with few points and most of the flow

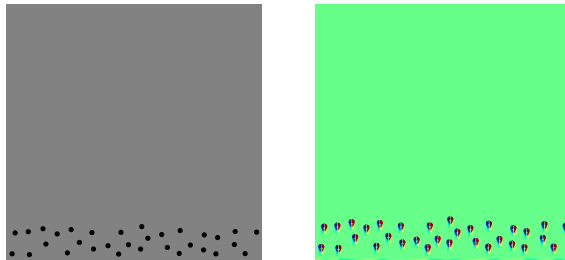


Figure 9: Bubble positions within the domain at $t = 0$ for simulation (a). Left: a sketch. Right the numerical vorticity field at $t=0.4$, where it is possible to appreciate the motion of the bubbles.

is described with very few points. On the other hand, for lower error tolerances, a large portion of the flow around the bubble, including the whole wake, appears to be described with the maximum number of points allowed, indicating that with that error threshold no difference is made in this region. This inability to discriminate the presence of gradients over large scales suggests a possible over-refinement.

The issue has been investigated more quantitatively looking at the dynamics of the three configurations. In Fig. 8a, we show the evolution of the rise velocity of the bubble, which is given by the Reynolds number in dimensionless form. The two low-tolerance grids show very little difference (less than 1%) in the rise velocity, whereas for the highest-tolerance grid the difference in rise velocity is of the order of 5%. This indicates that the three grids are sufficient to get a qualitative reproduction of the physics of the problem but that only the two more refined are at convergence.

In figure 8b, we display the evolution of the number of grid points with time for the three different grids. This gives a measure of the computational cost of each setup. From figure 8a, we can see that a transient is present with a duration of about $8 \div 10$ unit times. We should therefore expect that after that period of time, a stabilisation in the number of grid points would be reached too. That is what is observed for the intermediate grid. The coarse one attains a *plateau* too early, while on the contrary, on the fine grid the number of points keeps increasing monotonically. That seems to indicate again an over-refinement of the bubble, which results in an useless increase in the number of points and thus of computational time.

It is worth emphasising that there is a strong link between physical properties and numerical parameters and that this cannot be overlooked. While the simulation of a single bubble remains feasible even with the over-refined grid thanks to the adaptive mesh, it would not be possible to tackle a problem with many bubbles with the same grid. Moreover without the adaptive mesh even the single bubble case appears desperate at this large a Reynolds numbers. In contrast, using a coarse grid may make the computation easy but the results will be largely unreliable.

In the following simulations, we shall use the intermediate grid parameters, if not explicitly indicated.

6. Two-dimensional bubbly flows

In this section we show the results of a 2-dimensional bubble column configuration. We consider a square domain with the vertical direction z aligned with gravity, acting downward. The tank, of size $50d_b \times 50d_b$, is filled with a liquid and 32 initially spherical bubbles are placed at the bottom, in a region confined between $z = 0$ and $z = 8d_b$,

| Case | Ar | Bo | N | d_b/Δ |
|----------|------|------|-------|--------------|
| <i>a</i> | 100 | 0.12 | 4096 | 82 |
| <i>b</i> | 140 | 0.20 | 8192 | 164 |
| <i>c</i> | 313 | 0.56 | 16384 | 328 |

Table 6: Non-dimensional parameters for the 2-dimensional bubble column. N represents the grid resolution.

and are homogeneously distributed in the lateral direction y , while avoiding any initial bubble overlap, and with a minimum distance between them of 1 diameter. This results in a local volume fraction in the region $0 \leq z \leq 8$ of $\alpha \simeq 5\%$. The domain is closed at the bottom by a wall (no-slip boundary condition), and an outflow boundary condition is used at the top, while on the lateral sides the domain is periodic. At $t = 0$ both the liquid and the bubbles are at rest. A picture of the initial condition is shown in figure 9. The configuration is similar to that investigated experimentally in three dimensions (Riboux *et al.* 2010) and in a confined two dimensional configuration (Bouche *et al.* 2012, 2014).

The flow parameters are given by the non-dimensional Archimedes and Bond numbers, defined in the previous sections. The viscosity and density ratios are constant in all the simulations and their values are $\mu_l/\mu_b = 100$ and $\rho_l/\rho_b = 1000$. Three different simulations with bubbles of different diameters have been carried out, and the corresponding parameters are reported in table 6. In particular, the Ar number is within the range $Ar \simeq 100 - 300$, which corresponds to typical three-dimensional experiments (Riboux *et al.* 2010). Given that we consider a true 2D configuration, the regimes are possibly quite different from the 3D case with respect to the path instability of the single bubble (Tchoufag *et al.* 2014; Cano-Lozano *et al.* 2016b). Inspecting the trajectories, it appears that the cases (a) and (b) are within the stable regime, in which the trajectory of the undisturbed bubble is rectilinear. Case (c) is more complex and the trajectory is chaotic.

From a numerical point of view, in all the three cases we have used regularly spaced grids with different resolutions depending on the increasing bubble Reynolds number. A regular grid has been preferred to the adaptive one since in two dimensions the gain with adaptivity is not evident, and because a regular grid spacing facilitates the computation of statistical measures (spectra in particular). In any case, the resolution requirements to get physically-sound results have always been fulfilled, as highlighted in table 6.

In figure 10, we display the velocity of the bubbles as a function of time for cases (a) and (b). It can be observed that after a transient, of the order of $t_{\text{trans}} \sim 10$, the bubble swarm spreads and is stretched in the vertical direction. Bubbles are in general disturbed in their motion and some bubbles are affected by high levels of fluctuations with respect to the mean velocity of the front. Notably, a few bubbles even remain trapped in the wake region with a significantly lower vertical velocity. This is due mainly to the fact that 2D interactions are stronger and have a longer range than in 3D. This results in a more disturbed path of the bubbles in the wakes which can deviate significantly from vertical motion with non-trivial downward motion at some instants.

We now consider the energy spectra. Since the problem is non-homogeneous and non-stationary, particular care must be taken in the definition of the interrogation window.

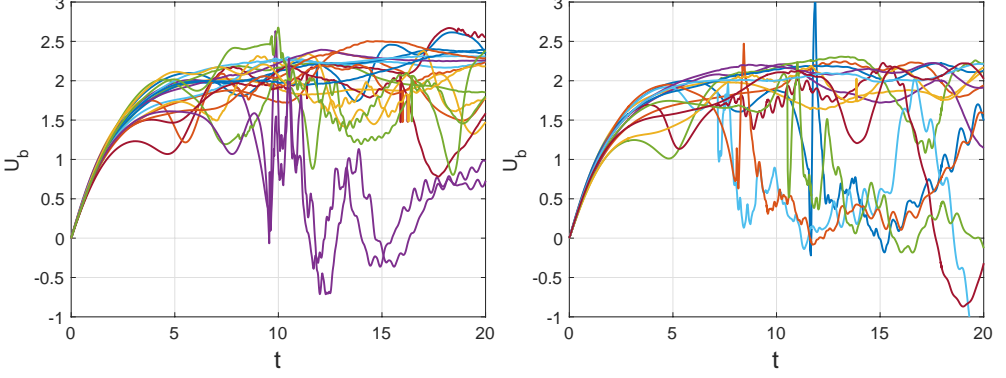


Figure 10: Velocities of the bubbles with respect to time. On left panel case (a), on right panel case (b).

In the experiment of Riboux *et al.* (2010), spectra are evaluated after the passage of the bubble swarm in a centred square box. In the present work, we have preferred to investigate also the region where bubbles are still present, since in our numerical simulations we can disentangle between the gas and liquid phase. Moreover, we have observed that waiting for the passage of all bubbles may result in wakes in the decaying regime, where most of the information is lost. The spectra $S_{ii} = \langle |\hat{u}_i|^2 \rangle$, where \hat{u}_i is the Fourier transform of the velocity fluctuation in the i direction, are evaluated separately for the vertical and the horizontal components. The transform is performed in the y direction, which can be considered as homogeneous, for both the components of the velocity and is then averaged in the z direction over windows of length $5d$, which have been found to be homogeneous to a good degree of approximation. Spectra obtained in this way for case (a) are displayed in figure 11. In all figures the energy is made non-dimensional with the corresponding standard deviation and on the x axis we show the wave number $k = 2\pi n/(50d_b)$ with $n = 1, \dots, N$. The value which corresponds to the bubble diameter is indicated by the vertical line. In Figure 11, we show both the spectra of the vertical and horizontal velocity fluctuations evaluated at different times, and on two different averaging windows, namely $15d_b \leq z \leq 20d_b$ and $20d_b \leq z \leq 25d_b$. It is worth remembering that time is made non-dimensional with $\sqrt{d_b/g}$. It can be seen that the spectral slope appears rather constant, without changes at some characteristic scale of the flow. A slope slightly steeper than -3 is identified and it appears robust with no significant time-dependence during the passage of bubbles. It can also be seen that after all bubbles have gone out from the interrogation window, the spectrum starts to decay exponentially. Moreover, the spectrum appears not yet well developed in the higher region between 20 and 25 diameters, and shows a steeper slope of $S_{ii} \sim k^{-4}$. No appreciable differences have been found between the horizontal and the vertical spectra, showing that both components dynamically distribute the energy in a similar manner.

In Figure ?? we show the vorticity field in the two portions of domain that have been used for the evaluation of the spectra at a fixed time $t = 14$. This vorticity field shows that the spectra scaling-law that has been found has little relation to the structures of the wakes, since in the upper window no significant interaction between the wakes is present, even though the resulting spectra are very close to those obtained in the lower window. This suggests that spectra are dominated by the coherent structures generated around the bubbles at the diameter scale. Smaller-scales dynamics appears to be largely

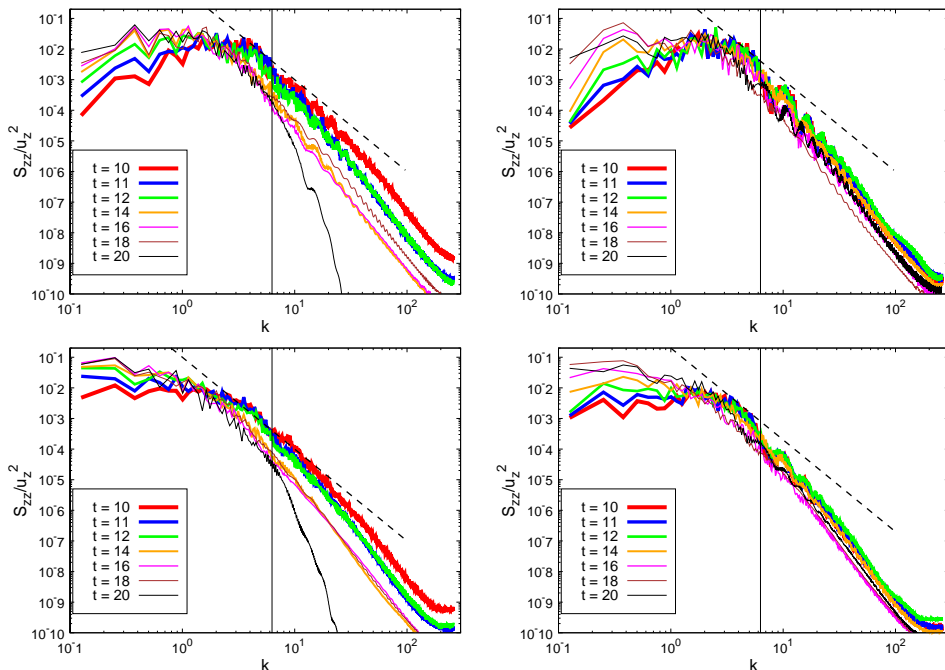


Figure 11: Spectra of the vertical (top line) and horizontal component (bottom line) of the velocity for bubbles with $Ar = 100$ and $Bo = 0.1$ evaluated at different times. On the left column the interrogation window is between 15 and 20 bubble diameters (in the vertical direction), while on the right column it is between 20 and 25. The dashed line represents the -3 slope. The vertical line corresponds to the bubble diameter.

sub-dominant. To make a link between the spectrum and the dynamics also in the viscous regime, we show in Figure ??c the vorticity field at $t = 20$ in the first window, that is when bubbles have long left and the flow is in the decaying regime. In this case, the flow appears to be laminar with only some fluctuations at the largest scale. In Figure 12 we show the vertical and horizontal spectra for the case (b). We can see a global behaviour similar to case (a), but with some notable differences: the spectrum is formed more rapidly, and in the space-time range considered the top window between 20 and 25 diameters displayed on the right column shows more stable spectra; moreover the spectra displays a -3 slope over roughly a decade in the range between one and ten bubble diameters. A steeper -4 scaling is found at smaller scales. From a dynamical point of view, Figure ?? shows the vorticity field for this case at $t = 20$. The field clearly suggests a stronger interaction between bubble wakes for this case.

Figure 13 shows energy spectra for case (c) at $Ar = 313$. It is interesting to observe that the scaling is substantially different with respect to the previous cases. At scales larger than the bubble diameter the spectrum appears more flat with a slope close to $-5/3$, while for smaller scales the slope is steeper. In the viscous range a k^{-4} scaling seems clear, and possibly in the crossover between the $-5/3$ and the -4 scaling there is still a range around the bubble diameter wavelength in which $S_{ii} \sim k^{-3}$. This behaviour remains a conjecture with the present data, since it is visible only at some times and the separation of scales is too small to draw any conclusion.

In any case, we think that the underlying physical mechanism at the origin of this

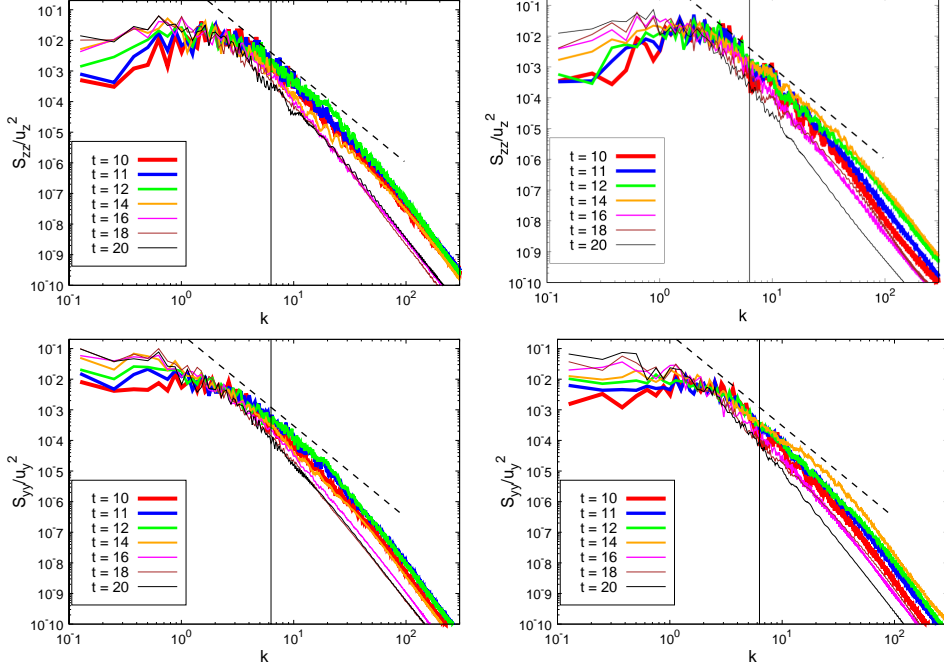


Figure 12: Spectra of the vertical (top line) and horizontal component (bottom line) of the velocity for bubbles with $Ar = 140$ and $Bo = 0.2$ evaluated at different times. On the left column the interrogation window is between 15 and 20 bubble diameters (in the vertical direction), while on the right column it is between 20 and 25. The dashed line represents the -3 slope. The vertical line corresponds to bubble diameter.

statistical behaviour is rather different. While, in cases (a) and (b) the spectrum is strongly dominated by the coherent structures of the wakes, here, because of the much higher Reynolds number, turbulent mechanisms are expected to play a more important role, even if the number of bubbles is not huge. The importance of interactions can be inferred also by the fact that, at variance with previous cases, no exponential viscous decay begins in the time window considered, and bubbles need more time to form the spectrum in the higher window. In fact, because of the strong interactions, bubbles are slowed down by their turbulent vortical dynamics. Therefore, the behaviour of the spectrum at the largest scales for this case should be related to a 2D inverse cascade. Notably, bubbly dynamics lead to an injection of energy at the scale of the bubble diameter, energy is then transferred at larger scales by the inverse cascade of energy, and a corresponding $-5/3$ scaling of the spectrum is displayed. The last steeper part should be related to viscous damping. The intermediate scaling, which possibly reveals a -3 scaling may be associated to the presence of vorticity at small scales generated in the wakes. That might in turn trigger a direct cascade of enstrophy. In order to emphasise the more complex structure of the flow at high Ar number, the Figure ?? shows the vorticity field at $t = 12$ in the window between 15 and 20 diameters. The strong interaction between wakes and the presence of dynamics at small scales is visible.

While energy spectra contain key information about the flow, it is not possible to disentangle from them the different mechanisms possibly leading to the same scaling.

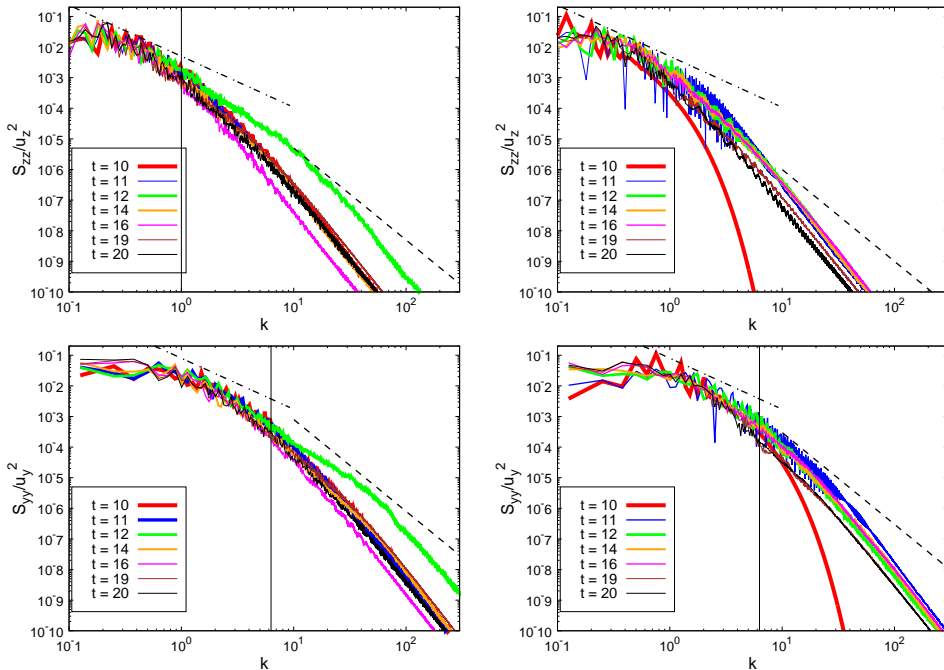


Figure 13: Spectra of the vertical component of the velocity for bubbles with $Ar = 313$ and $Bo = 0.56$ evaluated at different times. On the left column the interrogation window is between 15 and 20 bubble diameters (in the vertical direction), while on the right column it is between 20 and 25. The dashed line represents the -3 slope, the dashed-dotted line the $-5/3$ slope. The vertical line corresponds to bubble diameter.

For this reason, a scale-by-scale analysis is particularly useful. For that purpose, we apply a coarse-graining approach developed in a mathematical framework (Duchon & Robert 2000; Eyink & Sreenivasan 2006) and recently applied to different turbulent configurations (Chen *et al.* 2006; Xiao *et al.* 2009; Faranda *et al.* 2018; Dubrulle 2019; Valori *et al.* 2020). This approach is also linked to the filtering approach used in Large Eddy Simulations (Germano 1992). More specifically, we have applied this methodology to the velocity field, obtaining informations about the energy flux. The interesting advantage with respect to a spectral approach is that one can gain details also on the locality of the cascade, differentiating regions with positive or negative fluxes. We have applied a Gaussian filter to the velocity field in the same spatial windows considered above at different times. The filter is defined as:

$$G_l(\mathbf{r}) = \frac{1}{l} G\left(\frac{\mathbf{r}}{l}\right) \quad \text{with} \quad G(\mathbf{r}) = \sqrt{\frac{6}{\pi}} \exp(-6\mathbf{r}^2), \quad (6.1)$$

where l is the filter width. The application of the latter to the velocity field, yields the filtered velocity field:

$$\tilde{\mathbf{u}}_l(\mathbf{x}) = \int G_l(\mathbf{r}) \mathbf{u}(\mathbf{x} + \mathbf{r}) d\mathbf{r}. \quad (6.2)$$

Numerically, the filtering is performed in spectral Fourier space, multiplying the quantity to be filtered by the Fourier transform of the filter

$$\hat{G}_\ell(\mathbf{k}) = \exp(-k^2 \ell^2 / 24), \quad (6.3)$$

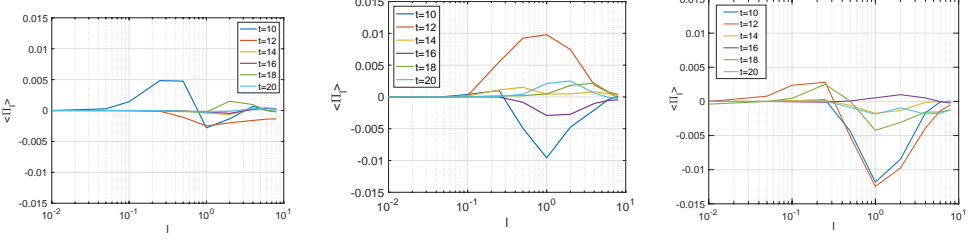


Figure 14: Mean energy flux with different filter lengths for the three simulations at different times. The spatial window is between $z = 15d_b$ and $z = 20d_b$, the same as in the computations of spectra. The length scale displayed in axis x is normalised with the diameter d_b , so that $\ell = 1$ corresponds to the bubble diameter.

and then transforming back into the physical space. The so-obtained filtered field contains only the contribution from eddies larger than ℓ and its transport equation can be obtained applying the filter to the Navier-Stokes equations. Analogously, the equation for the large-scale kinetic energy, $\tilde{e}_\ell = 1/2|\tilde{\mathbf{u}}_\ell|^2$, can be obtained:

$$\frac{\partial \tilde{e}_\ell}{\partial t} + \nabla \cdot \tilde{\mathbf{q}}_\ell = -\Pi_\ell - D_\ell, \quad (6.4)$$

where $\tilde{\mathbf{q}}_\ell$ is the transport term, D_ℓ is the large scale dissipation, and

$$\Pi_\ell = -\tilde{\mathbf{S}}_\ell : \boldsymbol{\tau} \quad (6.5)$$

is the local energy flux, related to the work made by large-scale shear against subgrid stress, and $\tilde{\mathbf{S}}_\ell$ and $\boldsymbol{\tau}$ are the filtered strain tensor and the subgrid scale tensor, defined as:

$$\tilde{\mathbf{S}}_\ell = \frac{1}{2} \left(\frac{\partial \tilde{u}_{\ell,i}}{\partial x_j} + \frac{\partial \tilde{u}_{\ell,j}}{\partial x_i} \right), \quad \boldsymbol{\tau} = (\widetilde{\mathbf{u}\mathbf{u}})_\ell - \tilde{\mathbf{u}}_\ell \tilde{\mathbf{u}}_\ell. \quad (6.6)$$

The term Π_ℓ identifies the presence of a local direct (positive) or inverse (negative) energy cascade according to its sign. If a spatial average is done at each different value of the filter width, one can find the average transfer of energy at each scale.

Results are reported in Figure 14 for the three different simulations. They show that for the two cases at lower Ar number, the flux is either not well defined, notably for $Ar = 100$ (the left panel) it is always around zero, and zero in average but with some strong event either for $Ar = 140$ (the central panel) in the range where the -3 scaling is exhibited. Instead, for the higher $Ar = 313$ (the right panel) number case the energy flux is mostly negative. It is worth remarking that since the problem is non-stationary, statistics depend on time, affecting both the shape and sign of the mean fluxes. In particular, in Figure 14c, we show the flux for the case $Ar = 313$ at different times. While important variability of the flux is encountered, the results show that the flux remains negative basically at all scales at almost each time and the negative peak is always at $\ell = d_b$. This analysis has thus pointed out the presence of a transfer of energy, which exhibits a maximum around the bubble diameter, and the presence of instantaneous local positive and negative energy fluxes over the whole domain. These results explain the physics underlying the different spectra scalings found. In the lower Ar cases bubbles generate wakes and perturb the flow but there is no robust instauration of collective turbulent motion. Some significant energy transfer may be encountered, but solely as an isolated event. The wake perturbations are in the range between 10 diameters (more or less the extension of the wake) and the diameter of the bubbles, and they have some tendency to create smaller vortices around

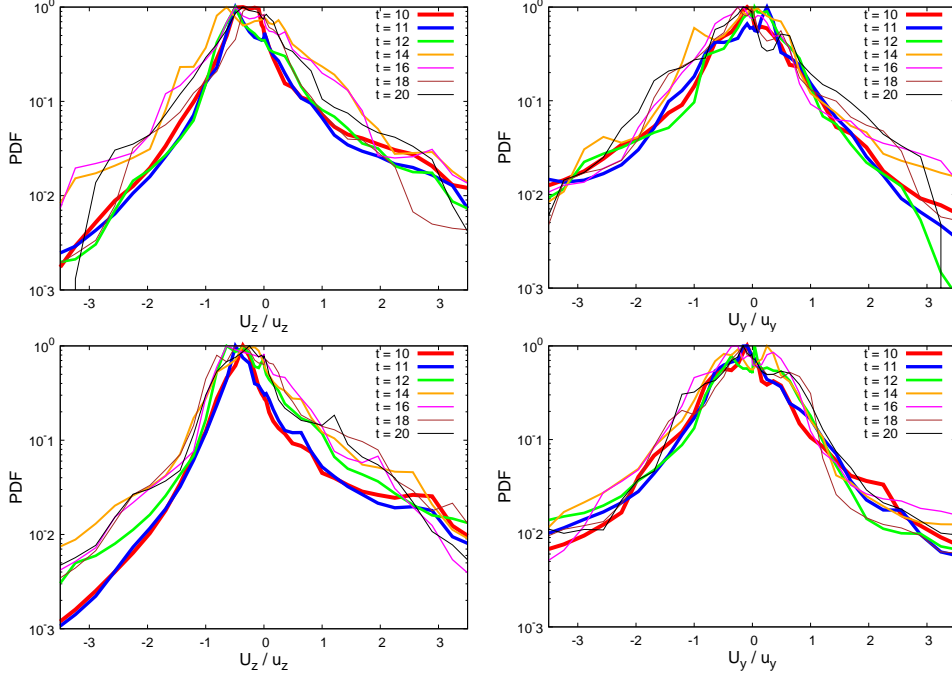


Figure 15: PDF of the velocity fluctuations in the vertical zz (left column) and lateral yy (right column) directions. Case (a) Bubbles at $Ar = 100$ and $Bo = 0.1$ (top panels); Case (b) Bubbles at $Ar = 140$ and $Bo = 0.2$ (low panels).

the bubbles, at least in the case $Ar = 140$. In the lower Ar case, the dynamics is found to be strongly attenuated by viscous effects. The $Ar = 313$ case turns out to be turbulent. The bubbles are able to inject enough energy at the bubble diameter scale to trigger an inverse cascade of energy with its spectral $-5/3$ counterpart. At smaller scales the situation is not well defined. The creation of smaller scales around the bubbles at some times is perceived as an injection of energy for the inverse cascade. At other times, the flux is basically zero at smaller scales and therefore a different spectrum may be found, notably the -3 spectrum typical of wakes and enstrophy production. However, in this range viscous damping is important and thus no neat scaling can be found except the viscous one. In order to get more insights about the cascade, we show in Figure ?? the spatial distribution of Π_l (with $l = 0.5, 0.1d_b$) for the case with $Ar = 313$ at $t = 12$. It can be noted how the regions of higher energy transfer are in the neighbourhood of the bubbles and how positive and negative areas are present over the whole domain. In particular smaller scales transfer is effective only in the vicinity of bubbles.

We consider now the issue of the fluctuation properties, looking at the probability density functions of the velocity fluctuations. Figures 15-16 show the PDFs of the two velocity components at various times for the three cases, in particular the lower Ar are grouped in figure 15. The first remark is that a time-dependent dynamics is noticeable. Even from a qualitative point of view, the PDFs display huge variations in the tails with respect to the time and to the window chosen, that is with respect to the particular region where they are calculated. Flow is clearly statistically unsteady and non-homogeneous in the vertical direction. Furthermore, fluctuations in the vertical direction are not isotropic, as can be seen from the strongly asymmetric PDFs on the left column. This is due to the fact that upward fluctuations are more probable because of the entrainment of the fluid in

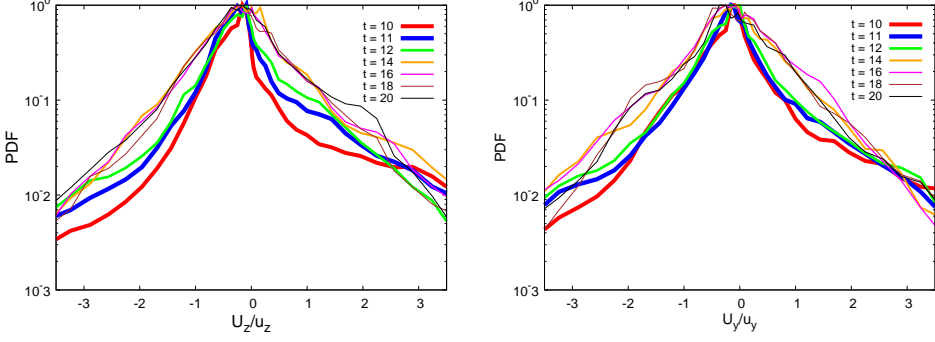


Figure 16: PDFs of the velocity fluctuations in the vertical zz (left panel) and lateral yy (right panel) directions. Bubbles with $Ar = 313$ and $Bo = 0.33$. The window is between $z = 15d_b$ and $z = 20d_b$.

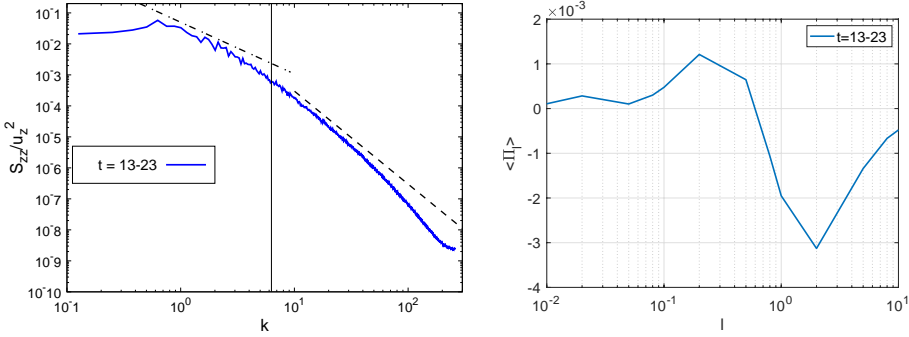


Figure 17: (a) Energy spectrum of vertical fluctuations against k . The spectrum is obtained by averaging over time between $t = 13$ and $t = 23$. The vertical line corresponds to bubble diameter. Time is normalized with the buoyancy timescale $\sqrt{d_b/g}$, for which the flow is found to be statistically stationary. (b) Mean energy flux, Eq. (6.5), with different filter lengths. The time-average is taken in the range $t = 13 - 23$ as in (a).

bubble wakes. The fluctuations of the horizontal component instead are more isotropic, resulting in symmetric PDFs, since bubble wakes are symmetric and the distribution of bubbles is uniform in the horizontal direction. Nevertheless, some differences can be pointed out between the lower Ar cases, figure 15, and the more turbulent one, figure 16. In the former cases, fluctuations show a tendency to become more symmetric and even gaussian in the final decaying regime. In the latter case, PDFs show some tendency to isotropisation but are non-gaussian at all times. Furthermore, with respect to other cases, the presence of more numerous extreme events in both directions is noticeable. This makes the flow locally isotropic at very small scales. This trend is another typical feature of turbulence cascades, as discovered by Kolmogorov (Monin & Yaglom 1975). The statistics of the velocity are thus consistent with the previous analysis based on spectra and vorticity fields.

To further corroborate the above picture, we have repeated the simulation of the case at $Ar = 313$ with periodic conditions on both directions. In this case, after a transient, a steady state is attained and furthermore the flow is statistically homogeneous in all directions. For this reason both spatial and time averages can be taken. Although periodic conditions are somewhat less realistic, in view of typical scales in experiments

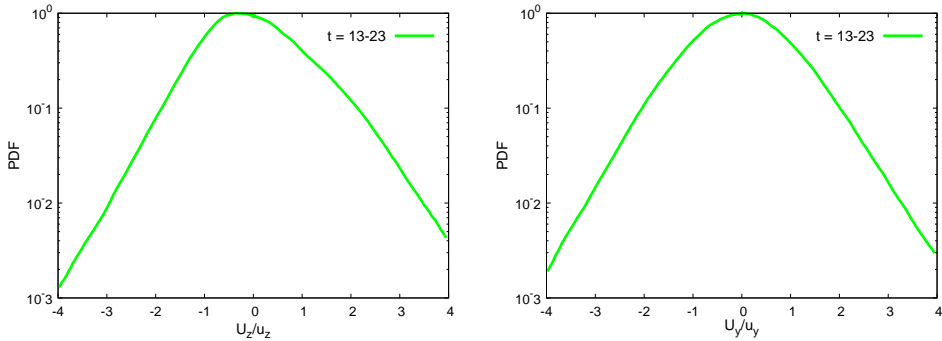


Figure 18: PDFs of the velocity fluctuations in the vertical zz (left panel) and lateral yy (right panel) directions in the periodical simulation. Average in time has been taken in the window $t = 13 - 23$.

the present results should share much similarity with experimental bubble swarms where homogeneous conditions can be met in certain regions of space (Riboux *et al.* 2010).

In figure 17a, we show the spectrum of vertical fluctuations and we can see that the periodic simulation confirm results obtained with the bubble column. In particular, a $k^{-5/3}$ scaling is displayed at scales larger than the bubble diameter. A k^{-3} scaling is possibly present in a tiny range around the bubble diameter and then a steeper slope typical of a viscous range is found. In figure 17b, the average flux is plotted against the filtering scale. Averaging over the same time window has been kept but statistical convergence has not been attained so that results are qualitative. The qualitative picture is clearly consistent however. In the range between 10 diameters and the bubble diameter an inverse cascade is present, At smaller scales there is no inertial energy flux, consistent with a possible enstrophy cascade. Given that bubbles are deformable, the peak at a scale slightly larger than the diameter may indicate that the typical bubble length is a little increased with respect to the beginning of the simulation.

In figure 18, the PDFs of the velocity fluctuations are showed. The time-average allows for a good statistical convergence of these quantities. PDFs are clearly not Gaussian and while the horizontal one is symmetric, the vertical one is skewed, showing anisotropy of fluctuations and the particular status of the vertical direction. Nonetheless, the skewness is less pronounced than in the lower Ar cases, confirming the tendency to recover locally isotropy at small scales in the turbulent regime.

7. Three dimensional bubble column

In this section, we show the results of the 3-dimensional bubble column configuration. The simulation domain and configuration are visualised in a snapshot in Figure 19. The bubble column is a direct extension of the previous 2-D numerical experiments, so that we consider a cubic domain with the vertical direction z aligned with gravity, acting downward; the tank, of size $50d_b \times 50d_b \times 50d_b$, is filled with a liquid and 256 initially spherical bubbles are placed at the bottom, in a region confined between $z = 0$ and $z = 3d_b$, and are homogeneously distributed in the lateral directions x , y , while avoiding any initial bubble overlap, and with a minimum distance between them of 1 diameter. This results in a local volume fraction in the region $0 \leq z \leq 3$ of $\alpha \simeq 2\% \div 4\%$. The domain is closed at the bottom by a wall (no-slip boundary condition), and an outflow boundary condition is used at the top, while on the lateral sides the domain

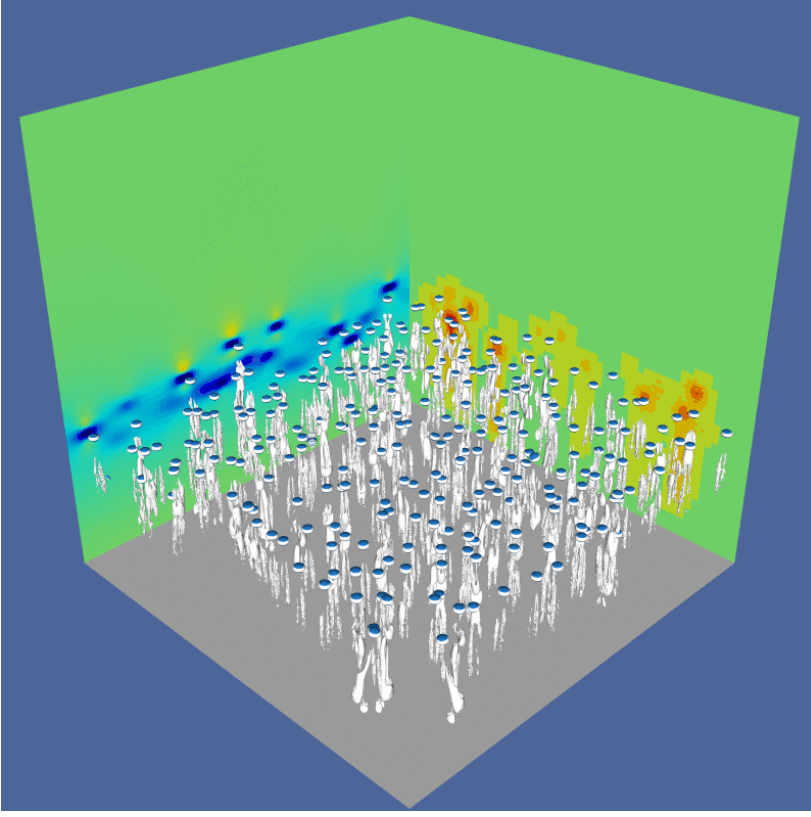


Figure 19: Snapshot of the 3D simulation at $t = 6$ after the release. The VOF field is showed with blue iso-surfaces and the λ_2 vorticity field is shown with grey contours. On the right wall is shown the level of mesh adaptation, while on the left panel the vertical velocity field.

is periodic. At $t = 0$ both the liquid and the bubbles are at rest. The dimensionless characteristic number of our numerical experiment are the following: $Ar = 185$; $Bo = 0.28$; $\rho_l/\rho_b = 800$; $\mu_l/\mu_b = 100$. The configuration is in many respects equivalent to that investigated experimentally in three dimensions by Riboux *et al.* (2010). At the level of qualitative picture, Figure 19 shows the instantaneous motion of the bubble at time $t = 6$, always made non-dimensional with the bubble buoyancy time $\sqrt{d_b/g}$. The bubbles have generated vorticity included in elongated wakes behind them which start interacting.

From the numerical point of view, an adaptive mesh has been used with a maximum possible refinement of $N = 4096$ cells in each direction, meaning a maximum resolution in terms of the bubble diameter of $d_b/\Delta = 82$. The grid is refined or coarsened relying on the errors on the volume fraction and on the velocity components, using as absolute thresholds for the refinement the values $e_f = 0.01$ and $e_v = 0.003$. The total number of computational cells grows in time because of the elongation of the wakes, starting from $N_{tot} \simeq 10^8$ to $N_{tot} \simeq 9 \cdot 10^8$ at $t = 12$. Consequently, also the number of CPUs is increased in time to maintain a well balanced parallelisation, attaining a final number of $N_{cpu} = 1536$. Note that using a non-adaptive mesh would require $4096^3 \approx 69 \times 10^9$ grid points.

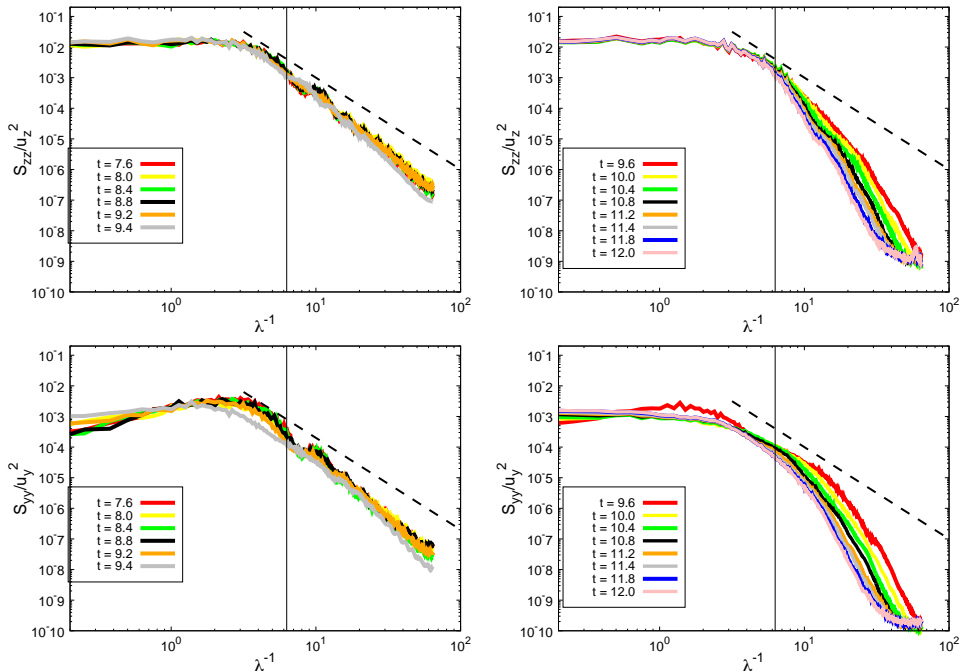


Figure 20: Spectra of the vertical (top line) and horizontal component (bottom line) of the velocity for bubbles with $Ar = 185$ and $Bo = 0.28$ evaluated at different times at $z = 25d_b$. The dashed line represents the -3 slope and the vertical line the bubble diameter. The curve is given to guide the eye.

In figure 20, we present the spectra of the vertical and horizontal components of the velocity computed in the horizontal plane at the middle of the domain $z = 25d_b$, at different times. To compute the spectra, we have interpolated the data on a regular grid. To avoid spurious errors, we have eliminated the highest wave-modes, so that spectra are calculated for 512 modes, although the maximum refinement is up to 4096 points. With respect to 2D simulations, the statistics evolve faster as highlighted by the rapid decay displayed between left panels and right panels in figure 20. In the same way, fields have been found to be non-homogeneous along the vertical direction z even on small distances of about $2 \div 3 d_b$, such that we have not performed any average over this direction, only average on the plane is performed. Both vertical and horizontal spectra contain the same physical information: when the bubbles go through the liquid, they agitate it generating significant fluctuations in the range $\lambda \in [10d_b, 0.1d_b]$, before being dissipated. In most of this range, the spectrum follows a power law with the expected scaling $S(k) \sim k^{-3}$. When the bubbles have left the spatial region under investigation, agitation decays rapidly, and an exponential fall-off is recorded. In particular, we have shown the results at $z = 25d_b$, since bubbles were inside at time $t = 7.6$, when we start to compute spectra, and left the horizontal plane at about $t = 9$. It is clear from the figures that a maximum is reached at around $t = 9.2$, before decaying. Comparing the dynamics in time of spectra in 2D and 3D, it is apparent that agitation is more persistent in the 2D case.

In order to qualitatively corroborate such analysis, we show in figure ?? the vorticity field on the same plane used to compute the spectra. This field allows to highlight the position of the bubbles and to visualise the generation of vorticity at the scale of the

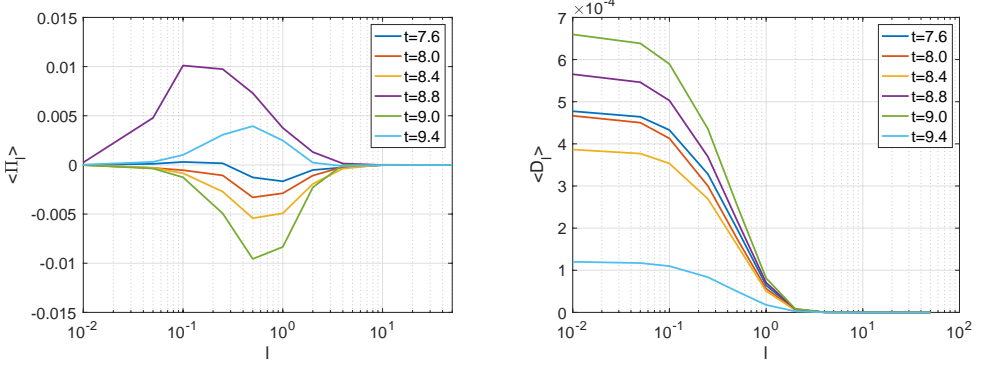


Figure 21: Mean energy flux at different filter lengths for the 3D simulation: (a) left panel, the energy flux; (b) right panel, the dissipative flux. Fluxes are computed at $z = 25d_b$, the same as for the computations of spectra. The length scale displayed on the x axis is normalised with the diameter d_b , so that $\ell = 1$ corresponds to the initial bubble diameter.

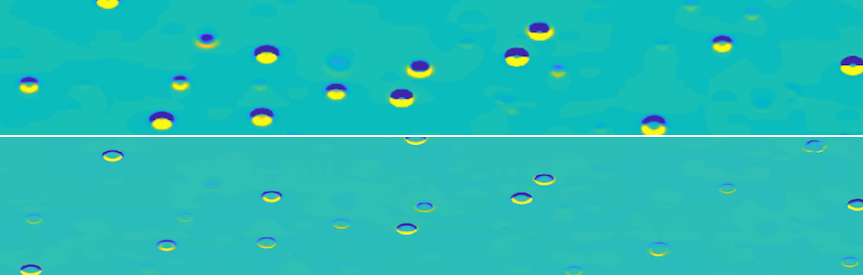


Figure 22: Local energy flux at $t = 9$ at $z = 25d_b$. In the upper panel the filter length is $l = 0.5d_b$, in the lower panel $l = 0.1d_b$. The color scale is the same in both panels.

diameter and slightly more. In some cases, it is apparent that different vortices have interacted, producing more complex structures.

In figure 21, we show the mean fluxes computed from the coarse-grained quantities defined in Eq. (6.5). Generally speaking, the scale-by-scale fluxes show a great variability in time, pointing out again the strong statistical unsteadiness of the flow. For this reason, statistics can be computed only at each time and therefore only a qualitative picture can be extracted meaningfully. The energy dynamics are non-trivial, with both inverse and direct cascades, with the direct cascade as dominant process. Furthermore, the inverse cascade concerns scales around the diameter and larger, whereas the direct cascade is triggered at scales of the order of the diameter, and involves about a decade of smaller scales. As expected, the dissipation of resolved scales is negligible at large scales and even at small scales, but in the dissipative range, as seen from 21b. It is important to remark that dissipation starts being significant for $\ell \approx d_b/2$, showing that fluctuations are mostly dissipated in the wakes generated by bubbles. It should be noted that at scales smaller than the diameter scale, there is roughly a balance between the dissipation and the energy flux, considering also the contribution from the dissipation of unresolved scales. In figure 22, we show a slice of the energy flux at two different scales, around the diameter and at a smaller scale. The pictures show that the energy flux and hence dissipation are concentrated in the wakes generated by the bubbles. Furthermore, these structures, initially of the size of the diameter, may become a little larger, indicating

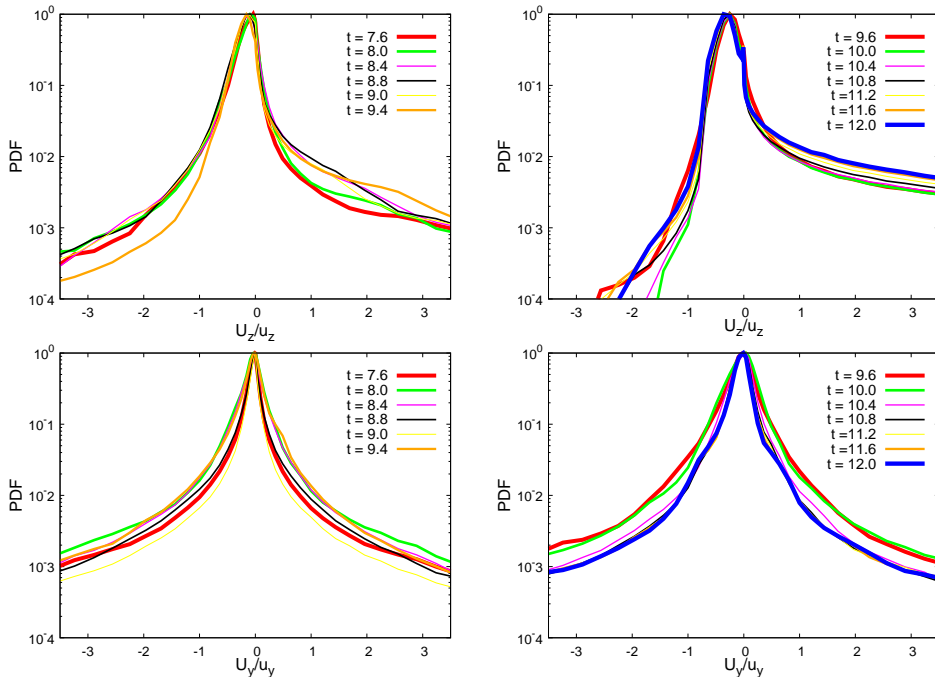


Figure 23: PDFs of the velocity fluctuations in the vertical zz (top panels) and lateral yy (bottom panel) directions, at different times.

the generation of larger eddies, and eventually are dissipated at small scales, where the imprint of the bubbles is still detectable.

Considering both spectra and fluxes, we deduce the following physical picture: bubbles generate wakes around the scale of the diameter; since the Reynolds is high, inside these structure smaller scales are formed and a cascade is triggered; moreover, different wakes have hydrodynamical interactions, which in turn help the triggering of the cascade, and also generate larger vortices, inducing a local transfer of energy from smaller to larger scales. Given that the flow is unsteady, both processes happen at the same time, and typically large structures are created injecting energy at large scales and the energy is then transferred rapidly to smaller scales to be dissipated. The agitation so induced around the diameter scale is eventually dissipated inside the wakes.

In figure 23, the Probability Density Function of the vertical and horizontal x velocity are presented (the y component does not present appreciable statistical differences), computed at several times. The statistics are calculated still at the horizontal plane $z = 25d_b$. We find the same characteristics reported in experiments (¹): the vertical velocity is strongly skewed, indicating a more important probability of having positive fluctuations, while the horizontal components are symmetrical. Furthermore, both components are non-gaussian, underlying the complex features of the bubble-induced agitation. Concerning the time-evolution, the figures display interesting features; bubbles enter this plane shortly before $t = 7.6$, first time in the figure, and the agitation is rapidly created, notably the skewness in the vertical component. Still, the passage of the bubbles increases this bubble-induced characteristic, which persists up to the time when bubbles have gone out from the plane (at $t \approx 10$). The horizontal component, displayed in the bottom panels, show a similar trend, but the fluctuations start decaying more rapidly.

This behaviour is consistent with the fact that wakes fall off more rapidly in the cross-stream direction than in the vertical one.

8. Discussion and Conclusions

In this work we have investigated several buoyancy-driven bubbly flows. A comparison with literature studies in the case of periodic arrays of rising bubbles has been done, to assess the accuracy and the performance of the numerical code used, namely the open-source code Basilisk. Overall we have found a very good agreement with both 2-d and 3-d literature results, where simulations were performed with different interface advection methods. We have then studied the oblique rise of buoyant bubbles in periodic arrays, confirming the recent results of Loisy *et al.* (2017), where an oblique path is obtained at certain values of the volume fraction.

Before performing simulations with many bubbles, we have studied some technical issues related to the numerics, in order to assess the numerical constraint needed to get accurate results. First we have evaluated the possibility of having coalescences in 2-d simulations with two raising bubbles at an initial distance of $1.5d$. We have found that the density ratio of the two fluids plays an important role and that to avoid excessive numerical coalescences it is necessary to have realistic densities. Moreover, we have also demonstrated that grid refinement is needed to resolve the film, thus recovering the correct levels of pressure that repel the bubbles. Otherwise, unphysical coalescence will take place. We have then studied in more detail the criteria for grid refinement, studying the 3-d rise of a single bubble to fix the parameters for the 3-d simulation with many bubbles.

The main message from this part of our work is that in order to obtain results which agree at a quantitative and even a qualitative level with experiments, it is necessary to fulfil the following criteria: (i) The density ratio has to be realistically high $\rho_l/\rho_b > 200$; (ii) The viscosity ratio should be also taken as the realistic one $\mu_l/\mu_b \approx 100$; (iii) The number of points used to resolve the bubbles must increase linearly with the Archimedes number (or the Reynolds number based on the raise velocity). As a rule of thumb, this number should be of the same order as the Ar number, $d_b/\Delta \sim Ar$. A numerical simulation which fails to fulfil these criteria, cannot be said a DNS, but should be considered as an implicit Large-Eddy-Simulation without sub-grid modelling. As we have shown, results may qualitatively depart from those of the well-resolved simulation.

We then performed computations of a two-dimensional bubble column at moderate and high Reynolds numbers and with a volume fraction of about 5% in the bubble layer. In this configuration, we have analyzed the velocity fluctuations in both phases finding different behaviours at different Reynolds numbers, even if the -3 slope of the spectra seems to be a robust feature of this type of flow, also in 2-d. As expected, PDFs show the strong anisotropy of the flow fluctuations in the vertical direction, while horizontal fluctuations are symmetric. A local scale-by-scale analysis of energy transfers performed in physical space has also shown the presence of energy fluxes at scales within two decades of the bubble diameter. In particular, the presence of an inverse cascade at scales larger than the diameter has been unveiled.

The same analysis has then been performed in a 3-D case, at $Ar = 185$ which corresponds to a Reynolds number consistent with experiments. The numerical simulations confirm the features of the liquid agitation showed experimentally (Riboux *et al.* 2010; Risso 2018).

Our scale-by-scale analysis allowed to single out the main mechanisms: (i) the bubbles are a source of energy fluctuations around the diameter scale; This input W_b is located at

the diameter size and is approximately constant and proportional to the work made by buoyancy: $W_b \sim \alpha g U_b$; (ii) the scale at which dissipation starts becoming important is of the order of the diameter, and the energy is dissipated in the wakes at smaller scales. This means that there is a range where these two fluxes $W_{\text{diss}} \approx W_b \rightarrow \nu(\delta u_\ell)^2/l^2 \sim \alpha g U_b$. This gives the scaling behaviour $\delta u_\ell^2 \sim l^2$, which means in spectral space $E(k) \sim k^{-3}$. The argument is similar to what already proposed for the spectral equation (Lance & Bataille 1991; Prakash *et al.* 2016). While the scaling behaviour appears to be fixed on dimensional grounds, the result shows that the field caused by bubble agitation is smooth at large wavenumbers, consistently with the wake model proposed by (Risso 2011). (iv) In two dimensions, since a direct cascade is absent, at larger scales than the diameter, where the dissipation is negligible, the energy budgets is $\Pi_\ell \sim W_b \approx \alpha g U_b$ which gives the Kolmogorov scaling $\delta u_\ell^2 \sim \ell^{2/3}$, or $E(k) \sim k^{-5/3}$, typical of an inverse cascade. In 3D, the instantaneous flux of energy towards large scales is present but not in average, where a direct cascade is observed.

A future development of the work would be to present and analyse the budgets of the momentum and energy equation in relation to the development of two-fluid models, that is Reynolds averaged Navier-Stokes (RANS). Indeed, the two-fluid model (Drew 1983; Drew & Passman 2006) probably represents the most widely adopted approach to describe the spatial and temporal evolution of gas-liquid flows in systems of practical relevance, due to its moderate computational cost. Unfortunately, it has been known for a long time that the numerical stability of the solution obtained from the two-fluid model depends on the characteristics of the underlying equations, which may be complex (Stuhmiller 1977; Ramshaw & Trapp 1978). In such a case, the equations are not hyperbolic and the discretized equations do not allow a grid-converged solution to be achieved. Unstable modes in the solution appear, severely affecting the model prediction and its sensitivity to grid refinement. To ensure the hyperbolicity of the system and therefore stability, an ad-hoc pressure term is usually introduced by hand (Prosperetti & Jones 1987). The shape of the term is yet controversial (Tiselj & Petelin 1997) and its properties have been extensively studied (Davidson 1990; Song & Ishii 2001). While the functional dependence on the volume fraction seems to be clearly established (Panicker *et al.* 2018), the multiplicative factors are unknown and may be found only from DNS or experiments. Therefore, the present DNS results could be used to analyse the momentum balance budget, and notably one should evaluate all the forces acting on the bubble in order to disentangle the contribution due to this interfacial term. Since this term is actually proportional to the gradient of the volume fraction $\nabla\alpha$, it is evident that this term is crucial when a jump in volume fraction is present, and this is precisely the case in a bubble column.

9. Acknowledgements

This work was granted access to the HPC resources of [TGCC/CINES/IDRIS] under the allocation 2019- [A0062B10759] attributed by GENCI (Grand Equipement National de Calcul Intensif). We thank Rodney Fox for fruitful discussions.

REFERENCES

- BALACHANDAR, S. & EATON, J. K. 2010 Turbulent dispersed multiphase flow. *Annu. Rev. Fluid Mech.* **42**, 111–133.
- BATCHELOR, GEORGE KEITH 2000 *An introduction to fluid dynamics*. Cambridge university press.
- BOUCHE, EMMANUELLA, ROIG, VÉRONIQUE, RISSO, FRÉDÉRIC & BILLET, ANNE-MARIE 2012 Homogeneous swarm of high-reynolds-number bubbles rising within a thin gap. part 1. bubble dynamics. *Journal of Fluid Mechanics* **704**, 211–231.
- BOUCHE, EMMANUELLA, ROIG, VÉRONIQUE, RISSO, FRÉDÉRIC & BILLET, ANNE-MARIE 2014 Homogeneous swarm of high-reynolds-number bubbles rising within a thin gap. part 2. liquid dynamics. *Journal of Fluid Mechanics* **758**, 508–521.
- CANO-LOZANO, JOSÉ CARLOS, MARTINEZ-BAZAN, CARLOS, MAGNAUDET, JACQUES & TCHOUFAG, JOËL 2016a Paths and wakes of deformable nearly spheroidal rising bubbles close to the transition to path instability. *Physical Review Fluids* **1** (5), 053604.
- CANO-LOZANO, JOSÉ CARLOS, TCHOUFAG, JOËL, MAGNAUDET, JACQUES & MARTÍNEZ-BAZÁN, CARLOS 2016b A global stability approach to wake and path instabilities of nearly oblate spheroidal rising bubbles. *Physics of Fluids* **28** (1), 014102.
- CHEN, SHIYI, ECKE, ROBERT E, EYINK, GREGORY L, RIVERA, MICHAEL, WAN, MINPING & XIAO, ZUOLI 2006 Physical mechanism of the two-dimensional inverse energy cascade. *Physical review letters* **96** (8), 084502.
- CHORIN, ALEXANDRE JOEL 1969 On the convergence of discrete approximations to the navier-stokes equations. *Mathematics of computation* **23** (106), 341–353.
- DAVIDSON, MALCOLM R 1990 Numerical calculations of two-phase flow in a liquid bath with bottom gas injection: the central plume. *Applied mathematical modelling* **14** (2), 67–76.
- DIOTALLEVI, F, BIFERALE, L, CHIBBARO, S, LAMURA, A, PONTRELLI, G, SBRAGAGLIA, M, SUCCI, S & TOSCHI, F 2009 Capillary filling using lattice boltzmann equations: The case of multi-phase flows. *The European Physical Journal-Special Topics* **166** (1), 111–116.
- DODD, MICHAEL S & FERRANTE, ANTONINO 2016 On the interaction of taylor length scale size droplets and isotropic turbulence. *Journal of Fluid Mechanics* **806**, 356–412.
- DREW, D.A. 1983 Mathematical modeling of two-phase flow. *Ann. Rev. Fluid Mech.* **15**, 261–291.
- DREW, DONALD A & PASSMAN, STEPHEN L 2006 *Theory of multicomponent fluids*, , vol. 135. Springer Science & Business Media.
- DUBRULLE, BÉRENGÈRE 2019 Beyond kolmogorov cascades. *Journal of Fluid Mechanics* **867**.
- DUCHON, JEAN & ROBERT, RAOUL 2000 Inertial energy dissipation for weak solutions of incompressible euler and navier-stokes equations. *Nonlinearity* **13** (1), 249.
- ERN, PATRICIA, RISSO, FRÉDÉRIC, FABRE, DAVID & MAGNAUDET, JACQUES 2012 Wake-induced oscillatory paths of bodies freely rising or falling in fluids. *Annual Review of Fluid Mechanics* **44**, 97–121.
- ESMAEELI, ASGHAR & TRYGGVASON, GRETAR 1998 Direct numerical simulations of bubbly flows. part 1. low reynolds number arrays. *Journal of Fluid Mechanics* **377**, 313–345.
- ESMAEELI, ASGHAR & TRYGGVASON, GRETAR 1999 Direct numerical simulations of bubbly flows part 2. moderate reynolds number arrays. *Journal of Fluid Mechanics* **385**, 325–358.
- ESMAEELI, ASGHAR & TRYGGVASON, GRÉTAR 2005 A direct numerical simulation study of the buoyant rise of bubbles at o (100) reynolds number. *Physics of Fluids* **17** (9), 093303.
- EYINK, GREGORY L & SREENIVASAN, KATEPALLI R 2006 Onsager and the theory of hydrodynamic turbulence. *Reviews of modern physics* **78** (1), 87.
- FARANDA, DAVIDE, LEMBO, VALERIO, IYER, MANASA, KUZAY, DENIS, CHIBBARO, SERGIO, DAVIAUD, FRANCOIS & DUBRULLE, BERENGÈRE 2018 Computation and characterization of local subfilter-scale energy transfers in atmospheric flows. *Journal of the Atmospheric Sciences* **75** (7), 2175–2186.
- GERMANO, M 1992 Turbulence: the filtering approach. *Journal of Fluid Mechanics* **238**, 325–336.
- HIRT, CYRIL W & NICHOLS, BILLY D 1981 Volume of fluid (vof) method for the dynamics of free boundaries. *Journal of computational physics* **39** (1), 201–225.
- VAN HOOFT, J ANTOON, POPINET, STÉPHANE, VAN HEERWAARDEN, CHIEL C, VAN DER LINDEN, STEVEN JA, DE ROODE, STEPHAN R & VAN DE WIEL, BAS JH 2018 Towards adaptive

- grids for atmospheric boundary-layer simulations. *Boundary-layer meteorology* **167** (3), 421–443.
- JAKOBSEN, HUGO A, LINDBORG, HÅVARD & DORAO, CARLOS A 2005 Modeling of bubble column reactors: progress and limitations. *Industrial & engineering chemistry research* **44** (14), 5107–5151.
- LAGRÉE, P-Y, STARON, LYDIE & POPINET, STÉPHANE 2011 The granular column collapse as a continuum: validity of a two-dimensional navier-stokes model with a μ (i)-rheology. *Journal of Fluid Mechanics* **686**, 378–408.
- LANCE, M & BATAILLE, J 1991 Turbulence in the liquid phase of a uniform bubbly air–water flow. *Journal of fluid mechanics* **222**, 95–118.
- LANDAU, LEV DAVIDOVICH & LIFSHITZ, EVGENII MIKHAILOVICH 1987 *Fluid mechanics*. Pergamon.
- LIAO, YIXIANG & LUCAS, DIRK 2010 A literature review on mechanisms and models for the coalescence process of fluid particles. *Chemical Engineering Science* **65** (10), 2851–2864.
- LOHSE, DETLEF 2018 Bubble puzzles: From fundamentals to applications. *Physical review fluids* **3** (11), 110504.
- LOISY, AURORE, NASO, AURORE & SPELT, PETER DM 2017 Buoyancy-driven bubbly flows: ordered and free rise at small and intermediate volume fraction. *Journal of Fluid Mechanics* **816**, 94–141.
- MAGNAUDET, JACQUES & EAMES, IAN 2000 The motion of high-reynolds-number bubbles in inhomogeneous flows. *Annual Review of Fluid Mechanics* **32** (1), 659–708.
- MARTÍNEZ-MERCADO, JULIÁN, PALACIOS-MORALES, CARLOS A & ZENIT, ROBERTO 2007 Measurement of pseudoturbulence intensity in monodispersed bubbly liquids for 10 ≤ Re ≤ 500. *Physics of Fluids* **19** (10), 103302.
- MATHAI, VARGHESE, LOHSE, DETLEF & SUN, CHAO 2020 Bubble and buoyant particle laden turbulent flows. *Annu. Rev. Condens. Matter Phys* **11**.
- MONIN, A. S. & YAGLOM, A. M. 1975 *Statistical Fluid Mechanics*. MIT Press, Cambridge, Mass.
- MOUGIN, GUILLAUME & MAGNAUDET, JACQUES 2001 Path instability of a rising bubble. *Physical review letters* **88** (1), 014502.
- PANICKER, NITHIN, PASSALACQUA, ALBERTO & FOX, RODNEY O 2018 On the hyperbolicity of the two-fluid model for gas–liquid bubbly flows. *Applied Mathematical Modelling* **57**, 432–447.
- POPE, S. B. 2000 *Turbulent Flows*. Cambridge University Press.
- POPINET, STÉPHANE 2003 Gerris: a tree-based adaptive solver for the incompressible euler equations in complex geometries. *Journal of Computational Physics* **190** (2), 572–600.
- POPINET, STÉPHANE 2009 An accurate adaptive solver for surface-tension-driven interfacial flows. *Journal of Computational Physics* **228** (16), 5838–5866.
- POPINET, STÉPHANE 2015 A quadtree-adaptive multigrid solver for the serre–green–naghdi equations. *Journal of Computational Physics* **302**, 336–358.
- POPINET, STÉPHANE 2018 Numerical models of surface tension. *Annual Review of Fluid Mechanics* **50**, 49–75.
- PRAKASH, VIVEK N, MERCADO, J MARTÍNEZ, VAN WIJNGAARDEN, LEEN, MANCILLA, ERNESTO, TAGAWA, YOSHIYUKI, LOHSE, DETLEF & SUN, CHAO 2016 Energy spectra in turbulent bubbly flows. *Journal of fluid mechanics* **791**, 174–190.
- PRINCE, MICHAEL J & BLANCH, HARVEY W 1990 Bubble coalescence and break-up in air-sparged bubble columns. *AIChE journal* **36** (10), 1485–1499.
- PROSPERETTI, A 2004 Bubbles. *Physics of fluids* .
- PROSPERETTI, A & JONES, AV 1987 The linear stability of general two-phase flow models?ii. *International journal of multiphase flow* **13** (2), 161–171.
- PROSPERETTI, ANDREA & TRYGGVASON, GRÉTAR 2009 *Computational methods for multiphase flow*. Cambridge university press.
- RAMSHAW, JOHN D & TRAPP, JOHN A 1978 Characteristics, stability, and short-wavelength phenomena in two-phase flow equation systems. *Nuclear Science and Engineering* **66** (1), 93–102.
- RIBOUX, GUILLAUME, RISSO, FRÉDÉRIC & LEGENDRE, DOMINIQUE 2010 Experimental

- characterization of the agitation generated by bubbles rising at high reynolds number. *Journal of Fluid Mechanics* **643**, 509–539.
- RISSO, FRÉDÉRIC 2011 Theoretical model for k -3 spectra in dispersed multiphase flows. *Physics of fluids* **23** (1), 011701.
- RISSO, FRÉDÉRIC 2018 Agitation, mixing, and transfers induced by bubbles. *Annual Review of Fluid Mechanics* **50**, 25–48.
- RISSO, FRÉDÉRIC & ELLINGSEN, KJETIL 2002 Velocity fluctuations in a homogeneous dilute dispersion of high-reynolds-number rising bubbles. *Journal of Fluid Mechanics* **453**, 395–410.
- ROGHAIR, IVO, MERCADO, JULIÁN MARTÍNEZ, ANNALAND, MARTIN VAN SINT, KUIPERS, HANS, SUN, CHAO & LOHSE, DETLEF 2011 Energy spectra and bubble velocity distributions in pseudo-turbulence: Numerical simulations vs. experiments. *International journal of multiphase flow* **37** (9), 1093–1098.
- ROGHAIR, IVO, VAN SINT ANNALAND, MARTIN & KUIPERS, HANS JAM 2013 Drag force and clustering in bubble swarms. *AIChE Journal* **59** (5), 1791–1800.
- SANGANI, ASHOK S 1987 Sedimentation in ordered emulsions of drops at low reynolds numbers. *Zeitschrift für angewandte Mathematik und Physik ZAMP* **38** (4), 542–556.
- SANKARANARAYANAN, K, SHAN, X, KEVREKIDIS, IG & SUNDARESAN, S 2002 Analysis of drag and virtual mass forces in bubbly suspensions using an implicit formulation of the lattice boltzmann method. *Journal of Fluid Mechanics* **452**, 61–96.
- SCARDOVELLI, RUBEN & ZALESKI, STÉPHANE 1999 Direct numerical simulation of free-surface and interfacial flow. *Annual review of fluid mechanics* **31** (1), 567–603.
- SHINNAR, REUEL & CHURCH, JAMES M 1960 Statistical theories of turbulence in predicting particle size in agitated dispersions. *Industrial & Engineering Chemistry* **52** (3), 253–256.
- SONG, JINHO & ISHII, MAMORU 2001 The one-dimensional two-fluid model with momentum flux parameters. *Nuclear Engineering and Design* **205** (1-2), 145–158.
- STUHMILLER, JH 1977 The influence of interfacial pressure forces on the character of two-phase flow model equations. *International Journal of Multiphase Flow* **3** (6), 551–560.
- TCHOUFAG, JOËL, MAGNAUDET, JACQUES & FABRE, DAVID 2014 Linear instability of the path of a freely rising spheroidal bubble. *Journal of Fluid Mechanics* **751**.
- TISELJ, IZTOK & PETELIN, STOJAN 1997 Modelling of two-phase flow with second-order accurate scheme. *Journal of Computational Physics* **136** (2), 503–521.
- TOSCHI, F & BODENSCHATZ, E 2009 Lagrangian properties of particles in turbulence. *Annual Review of Fluid Mechanics* **41**, 375–404.
- TRYGGVASON, G, SCARDOVELLI, R & ZALESKI, S 2011 *Direct Numerical Simulations of Gas-Liquid Multiphase Flows*. Cambridge University Press.
- VALORI, VALENTINA, INNOCENTI, ALESSIO, DUBRULLE, BÉRENGÈRE & CHIBBARO, SERGIO 2020 Weak formulation and scaling properties of energy fluxes in three-dimensional numerical turbulent rayleigh-bénard convection. *Journal of Fluid Mechanics* **885**.
- XIAO, Z, WAN, M, CHEN, S & EYINK, GL 2009 Physical mechanism of the inverse energy cascade of two-dimensional turbulence: a numerical investigation. *Journal of Fluid Mechanics* **619**, 1–44.
- ZENIT, ROBERTO, KOCH, DONALD L & SANGANI, ASHOK S 2001 Measurements of the average properties of a suspension of bubbles rising in a vertical channel. *Journal of Fluid Mechanics* **429**, 307–342.